Tampere University

Markus Hiekkamäki

UNITARY TRANSFORMATIONS OF SPATIAL MODES FOR QUANTUM EXPERIMENTS

Faculty of Engineering and Natural Sciences
Master's thesis
November 2019

ABSTRACT

Markus Hiekkamäki: Unitary transformations of spatial modes for quantum experiments
Master's thesis
Tampere University
Degree programme of science and engineering
November 2019

Spatial modes have attracted a lot of attention in the quantum optics community because of their possible application in high-dimensional quantum bits, i.e. qudits. One crucial task in quantum communication and computation applications, is the ability to perform unitary transformations on these qudits. However, arbitrary unitary transformations between full-field spatial modes have not been realized so far. Thus, in order to bring spatial modes closer to communication and computation applications, methods for performing these transformations need to be devised.

In this thesis, we introduce a method for generating these unitary transformations. The method is based on multi-plane light conversion (MPLC), where the spatial structure of light is transformed through multiple consecutive transverse-phase modulations. The method we use for generating these task specific phase-modulations is called wavefront matching (WFM).

This thesis consists of three main sections. First, we will introduce some necessary theory behind high-dimensional quantum-states and single photons. We will also explore some theory behind the generation of single photons and introduce light's spatial modes in more detail. Second, we will introduce WFM along with other methods we needed for testing the unitary transformations experimentally. Finally, we will experimentally test the mode transformations in a spatial mode filter and in multi-mode transformations. We apply the mode filter in quantum key distribution (QKD) and quantum state tomography (QST) measurements, and we implement different high-dimensional quantum gates using the multi-mode transformations. Additionally, we introduce a method of potentially observing two-photon interference with these unitary transformations.

With the mode filter, we achieved error rates below five percent and in the QKD application we measured a theoretical data transmission rate of 1.98 bits per measured photon. With the quantum gates, we achieved accuracies of up to 98% in all mutually unbiased bases (MUBs). The results shown in this thesis demonstrate the efficiency and unitarity of WFM in a broad set of different tasks. All the shown tasks are important in high-dimensional quantum communication and computation, and hence we believe that WFM will become an important tool in high-dimensional quantum information processing. We also give an outlook on how WFM could potentially be improved, and list some additional tasks, in which WFM could be useful. We believe that the broad applicability of WFM will enable some unexplored quantum information or photonics applications.

Keywords: quantum optics, high-dimensional, qudits, spatial modes, unitary transformations

TIIVISTELMÄ

Markus Hiekkamäki: Valon etenemismuotojen unitaarisia muunnoksia kvanttimekaanisille kokeille
Diplomityö
Tampereen yliopisto
Teknis-luonnontieteellinen tutkinto-ohjelma
Marraskuu 2019

Valon etenemismuodot ovat herättäneet paljon mielenkiintoa kvanttioptiikan alalla. Tämä mielenkiinto johtuu suurimmaksi osaksi niiden moniulotteisesta tila-avaruudesta, jota voidaan hyödyntää korkeaulotteisissa kvanttibiteissä eli kuditeissa (eng. qudit). Yksi tärkeä operaatio kvanttikommunikaatiossa ja -laskennassa on näiden bittien unitaarinen muuntaminen. Jotta etenemismuotoja voidaan hyödyntää kaikissa näissä sovelluksissa, täytyy niiden välillä pystyä tekemään lähes mielivaltaisia unitaarisia muunnoksia. Toistaiseksi näitä muunnoksia ei ole pystytty kuitenkaan toteuttamaan kaikille valon (eli fotonien) poikittaisrakenteille (eli etenemismuodoille).

Tässä diplomityössä esitämme yhden tavan generoida lähes mielivaltaisia unitaarisia muunnoksia etenemismuodoille. Menetelmä, jolla toteutamme nämä muunnokset perustuu valon rakenteen muuttamiseen monella tasolla (eng. Multi-plane mode conversion eli MPLC). MPLC:ssä fotonien poikittaisrakennetta muokataan monen peräkkäisen avaruudellisen vaiherakennemuunnoksen avulla. Nämä vaiherakennemuunnokset optimoidaan simulaatioalgoritmin avulla, jota kutsutaan aaltorintaman sovittamiseksi (eng. wavefront matching eli WFM).

Tämä diplomityö koostuu kolmesta eri osiosta. Ensimmäisessä osiossa esitellään kvanttitilojen ja yksittäisten fotonitilojen taustalla olevaa teoriaa. Näiden lisäksi ensimmäisessä osiossa käsitellään teoriaa yksittäisten fotonien tuottamisen taustalla ja esitellään fotonien poikittaisrakenteeseen liittyvät etenemismuodot. Toisessa osiossa käydään läpi WFM algoritmi yksityiskohtaisesti, sekä esitellään laitteita ja metodeja, joita tarvitaan työn kokeellisessa osiossa. Lopuksi WFM:llä toteutettuja unitaarisia muunnoksia testataan kokeellisesti, etenemismuotosuotimena ja laitteena, joka pystyy moneen samanaikaiseen muunnokseen. Suodinta testataan eräässä kvantti-kryptograafisessa tehtävässä (Quantum Key Distribution eli QKD) ja kvanttitomografiassa (eng. Quantum State Tomography eli QST). Monen muodon muunnoksia testataan rakentamalla muunnoksista korkeaulotteisia kvanttiportteja eri etenemismuotojen välillä. Näiden lisäksi työn lopussa esitellään mittalaitteisto, jolla voitaisiin tutkia kahden fotonin interferenssiä näitä unitaarisia muunnoksia hyödyntäen.

Etenemismuotosuotimella tehdyissä mittauksissa saavutettiin alle viiden prosentin virhetaajuus, ja QKD:ta testattaessa saavutettiin teoreettinen datansiirtonopeus, joka oli noin 1.98 klassista bittiä per fotoni. Moniulotteisilla loogisilla porteilla päästiin jopa 98% muunnostarkkuuksiin kaikissa keskenään tasa-arvoisissa kannoissa (eng. Mutually Unbiased Basis eli MUB). Nämä tulokset kertovat WFM:n tehokkuudesta ja unitaarisuudesta. Ne myös osoittavat kuinka tätä menetelmää voidaan hyödyntää useissa eri kvantti-informaatioon perustuvissa sovelluksissa. Tämän takia, WFM tulee varmasti olemaan tärkeä osa moniulotteista kvanttikommunikaatiota ja -laskentaa tulevaisuudessa. Työn lopussa listataan vielä mahdollisia tapoja parannella WFM menetelmää, ja mahdollisia tehtäviä, joissa sitä voisi hyödyntää. Listattujen esimerkkien lisäksi, WFM:n tehokkuus ja monipuolisuus tulee vielä mahdollistamaan joitain tutkimattomia kvanttioptiikan ja fotoniikan sovelluskohteita.

Avainsanat: kvanttioptiikka, korkeaulotteinen, kuditti, etenemismuodot, unitaarinen muunnos

PREFACE

This thesis was done in the Experimental quantum optics group of Tampere University during the year 2019. I would like to thank the Photonics Laboratory of Tampere University for this amazing opportunity of working on photonics research. Especially, I want to thank our group leader Robert Fickler for helping me understand and study the quantum nature of light in a very open and encouraging environment. Additionally, I appreciate all of the discussions and feedback I've had with the other members of the Experimental quantum optics group, along with the helpful and talkative people of SK114. I also want to thank Florian Brandt, Frédéric Bouchard, and Marcus Huber who collaborated with us in some of the work performed during this thesis.

I'm also grateful for Mona, who pulled me out of the laboratory every once in a while and supported me during the course of this thesis. Also, I'm thankful for all of the help, motivation, insight, and positivity I've received from Tommi, Timo, and Jussi, during our years of studying in Hervanta. Finally, I would like to thank my Mum and Dad for always encouraging and helping me with everything, and trusting in my abilities more than I trust in them myself.

In Tampere, 4th November 2019

Markus Hiekkamäki

CONTENTS

LIST OF SYMBOLS AND ABBREVIATIONS

HG_n^m	Hermite-Gaussian mode with quantized mode numbers n (vertical) and m (Horizontal).
LG_p^l	Laguerre-Gaussian mode with quantized mode numbers l (azimuthal) and p (radial).
$\langle\Psi\|$	bra
χ	Electric susceptibility
δ_{ij}	Kronecker delta
$\hat{\rho}$	State density operator
$\hat{a}$	Quantized field annihilation operator
$\hat{a}^\dagger$	Quantized field creation operator
$\|A\rangle$	Antidiagonal polarization
$\|D\rangle$	Diagonal polarization
$\|H\rangle$	Horizontal polarization
$\|L\rangle$	Left circular polarization
$\|R\rangle$	Right circular polarization
$\|V\rangle$	Vertical polarization
$\|\Psi\rangle$	ket
$\|\alpha\rangle$	Coherent light state
$\|n\rangle$	Fock-state or number-state
$\overline{n}$	Average photon number
ρ	Radius in cylindrical coordinates
φ	Azimuthal angle in cylindrical coordinates
$\underline{\mathbf{B}}$	Magnetic field density vector
$\underline{\mathbf{E}}$	Electric field vector
$\underline{\mathbf{x}}$	Position vector
$c.c.$	Complex conjugate
m	Mass
t	Time
w	Gaussian beam radius
w_0	Gaussian beam waist

z_R	Rayleigh range
APD	Avalanche photodiode
BS	Beamsplitter
CNOT	Controlled not
DFG	Difference frequency generation
EM	Electro-magnetic
FBS	Fiber beamsplitter
HG	Hermite-Gauss
HOM	Hong-Ou-Mandel
HWP	Half wave plate
LG	Laguerre-Gauss
MPLC	Multi-plane light conversion
MUB	Mutually unbiased basis
OAM	Orbital angular momentum
PBS	Polarizing beamsplitter
PPS	Photon pair source
QKD	Quantum key distribution
QPM	Quasi-phase-matching
Qudit	d-dimensional quantum bit (compare qubit for 2 dimensions).
SAM	Spin angular momentum
SHG	Second harmonic generation
SLM	Spatial light modulator
SMF	Single mode fiber
SPDC	Spontaneous Parametric Down-Conversion
TPA	Two-photon amplitude
TS	Transverse-spatial
WFM	Wavefront matching

1 INTRODUCTION

Along with the growth of quantum computing, communication methods utilizing the quantum states of photons have been gaining in popularity. Even though the most common encoding in these quantum communication applications has been the polarization degree of freedom [1, 2], there is a set of different, higher-dimensional quantized state spaces gaining popularity during the last decades. One of these high-dimensional state spaces is the transverse-spatial degree of freedom of light beams, that has potential in classical and quantum communication tasks as well as other quantum information schemes. Some of these classical communication schemes that utilize the transverse-spatial structures, have achieved transmission rates of up to a terabit per second [3]. In these classical applications, spatial modes are most commonly harnessed as separate parallel channels for data-streams [3], similarly to e.g. wavelength [4], that are used to increase the achievable transmission bandwidth. It is also possible to encode more than two data values onto a photon using these structures, since there are infinite sets of these mutually orthogonal modes. This approach is more popular in quantum communication tasks [3]. The high-dimensionality of these modes can then be harnessed in different types of single photon communication [5].Among the most interesting properties of these high-dimensional quantum bits, i.e. qudits, is the increased robustness to noise and eavesdropping in totally secure quantum communication channels [6, 7]. However, real world testing of these quantum communication schemes is still in its infancy, even though some tests have been performed, e.g. [8, 9, 10]. Nevertheless, new and more compact methods for generating, measuring and manipulation these qudits are needed for widespread adoption of these schemes.

In addition to their robustness in communication schemes, high-dimensional state spaces have shown promise in new types of computational algorithms [11, 12]. These computational algorithms require a way to transform these spatial modes in a unitary way. Thus far however, only a limited number of unitary transformations of spatial modes are known, and these methods only utilize one degree of freedom (azimuthal) from the transverse-spatial light modes [13, 14]. It would be highly desirable to extend these protocols to include the whole transverse-spatial structure in order to enable novel high-dimensional computational schemes and increase the qudit sizes. Additionally, to truly enable high-dimensional computing using spatial modes, a method to produce arbitrary unitary transformations for single photon spatial modes is required.

Our task was to examine a new method of generating arbitrary unitary transformations of single photon spatial modes. The ambitious end goal was to observe two-photon interference in the spatial mode degree of freedom, instead of the path degree of freedom. To achieve this, we would need to build a beamsplitter-like unitary transformation for a two-dimensional set of spatial modes.

Before doing this experiment though, we implemented some other important tasks with this unitary transformation method. These tasks included a new unitary mode-filtering technique, capable of near-perfectly measuring the total spatial mode structure of light, and optical quantum gates that take advantage of the high-dimensional state space. Our method for realizing these tasks was a multi-plane light conversion (MPLC) technique, that has been popular in spatial mode multiplexing and de-multiplexing [15]. In these multi-plane light conversion techniques spatial modes are gradually transformed by introducing transverse phase-modulations on the light beam on multiple consecutive planes. We obtained these phase-modulations through a new method adopted from waveguide designing, that is called wavefront matching (WFM). For free-space operation, this method was introduced by Fontaine et al. in [16].

We were able to successfully realize the near-perfect mode-filter and high-dimensional quantum gates. These arbitrary unitary quantum gates were also published as a part of a separate article [17]. Both tasks utilized the full transverse-spatial field of light, and as such are an important addition to other work involving high-dimensional spatial modes in quantum information tasks. We also built and simulated all the necessary parts for measuring the two-photon (or Hong-Ou-Mandel) interference in the transverse-spatial degree of freedom. However, actually observing this result needs more time, and thus it didn't fit into the limited time-frame of this thesis.

In this thesis, we will first introduce some relevant fundamental concepts, such as single photons, transverse-spatial modes, and optical nonlinearities that are required for generating pairs of single photons. Then we will introduce the WFM algorithm in detail, along with some important experimental devices and methods we used in our experiments. Next, we will introduce the quantum information tasks, which we implemented with our experimental setups. Finally, we will introduce the experimental setups we built along with the results of the measurements.

2 THEORY

In this thesis we will be discussing classical light, as well as single photons. Hence, in this chapter we will give a short introduction in to the quantization of the light, and how different light states can be described using this quantization. Second, we will describe the underlying theory behind the way we generated our heralded single photons and photons pairs, i.e. we will describe nonlinear light-matter interactions. More specifically we will focus on the nonlinear process of spontaneous parametric down-conversion (SPDC). After this, we will discuss two-photon interference or Hong-Ou-Mandel (HOM) interference in more detail, in order to understand how we could harness spatial-mode conversions for single beamline HOM interference. Finally, we will give some background on the orthogonal transverse-spatial modes of light that we are going to section into usable Hilbert space subsets for our unitary spatial mode transformations.

2.1 Quantized light

The quantization of light as particles was already postulated by Einstein in 1905, using Planck's discrete energy distribution for black-body radiation as a starting point [18]. Since then, the mathematical descriptions for single photon states has evolved from just relating the photon energy with the frequency of light. In this section we will shortly explain some of the quantum mechanical notations used throughout this thesis and introduce a more modern and simpler way to describe single photon states. Due to limited space we restrict ourselves to a very surface level analysis of quantized fields. Hence, for a more in-depth analysis there are books covering the topic, e.g. Gerry's and Knight's book [19] that we will be mostly using as a reference in this chapter.

2.1.1 Quantum states

In the system of notating that we will be using here, any arbitrary pure quantum state can be described by a so-called ket $|\Psi\rangle$. Furthermore, these arbitrary states $|\Psi\rangle$ can be described as a superposition constructed from a set of orthogonal states $|\psi_d\rangle$, $d \in \{1,2,...,N\}$, that form a complete Hilbert space basis of dimension N. Because of this, ket's are often represented as complex vectors in a specific Hilbert space, where each dimension of the vector corresponds to a certain state of the system. The orthogonality of two different states can be tested with the inner product that is defined in these discrete Hilbert spaces as $\langle\psi_d|\,\psi_g\rangle = \langle\psi_d|\,\psi_g\rangle^* = \delta_{dg}$ where the notation $\langle\psi_d| = |\psi_d\rangle^\dagger$ is called a bra [20], * signifies a complex conjugate, and the † notation denotes a

Hermitian conjugate. If the two states are identical the inner product is 1, and two orthogonal states have an inner product of 0. Additionally, a set of these basis states can be finite or infinite depending on the property of the system they are describing.

One example of a complete set of basis states, describing one of the simplest Hilbert spaces are the horizontal and vertical polarizations, $|H\rangle$ and $|V\rangle$. This means that polarization is a two-dimensional Hilbert space and can be fully described by two states. Hence, with these two polarization states one can describe any arbitrary polarization by introducing amplitude and phase differences between these two states. In quantum information tasks, these two-dimensional bases form qubits, or quantum bits, because we can have one state representing a zero $|0\rangle$ and a state orthogonal to it representing a one $|1\rangle$. The quantumness of these bits comes from the quantum properties we can achieve when constructing e.g. superpositions out of these bits.

Using a complete set of orthonormal states $|\psi_d\rangle$, any coherent superposition state can be expressed using the notation $|\Psi\rangle = \sum_d c_d |\psi_d\rangle$, where c_d are complex coefficients [20]. The superposition states $|\Psi\rangle$ are normalized such that $\sum_n |c_d|^2 = 1$. These complex coefficients c_d would then be the amplitudes our previously mentioned ket vectors have on each dimension d of the vector. A concrete example using our polarization states would be diagonal polarization constructed as a superposition of the horizontal and vertical polarizations $|D\rangle = \frac{1}{\sqrt{2}}(|H\rangle + |V\rangle)$ or in the vector notation

$$|D\rangle = \frac{1}{\sqrt{2}} \begin{bmatrix} 1 \\ 1 \end{bmatrix}. \tag{2.1}$$

Besides the two-dimensional polarization state space, there naturally exist higher dimensional examples, but we restrict our self to the polarization state space at first, due to its simplicity.

However, the notation shown above is only accurate for systems that are in a fully coherent superposition of these orthogonal states, also called pure states. As the framing suggests, this means that there are also incoherent mixtures of states, often called mixed states, that cannot be described by these pure states. These mixed states are a classical probabilistic mixture of different constituent states. One example of a pure state is the previously shown diagonal polarization $|D\rangle$ state. This state can be interpreted as a different state compared to its constituent states, meaning that we can measure the $|D\rangle$ state in a separate basis, i.e. the diagonal anti-diagonal polarization basis where the second basis vector is the anti-diagonal state $|A\rangle = {}^1/\sqrt{2}(|H\rangle + |V\rangle)$. In this $|D\rangle, |A\rangle$-basis the measurement is well defined, i.e. we measure $|D\rangle$ with a probability of one, while in the $|H\rangle, |V\rangle$-basis the outcome of a possible measurement is random. For a similar incoherent mixture of $|H\rangle$ and $|V\rangle$, the outcome is random for a measurement in either basis. In experiments, this would mean that with a pure state $|D\rangle$ we would measure this exact diagonal polarization for every photon in this state, e.g. by using a linear polarizer "rotated diagonally". However, for a similar statistical mixed state of half $|H\rangle$ and half $|V\rangle$, we would only measure the $|D\rangle$ state 50% of the time. This is because in the probabilistic mixture, the state is either $|H\rangle$ or $|V\rangle$ just with a certain probability for both, and our measurements just reveal in which the state was.. Whereas in the coherent diagonal-polarization state, the constituent states sum up to form a different state.

We can describe a fully mixed state by a state density operator of the form

$$\hat{\rho} = \sum_d |\psi_d\rangle\, p_d\, \langle\psi_d|\,, \tag{2.2}$$

where p_d is the probability of the system being in one of the orthogonal states $|d\rangle$. The probabilities p_d have to also sum up to unity $\sum_d p_d = 1$, as can be expected for a probabilistic mixture. If one calculates the expectation value of this density operator with any orthogonal basis state, one obtains the probability with which the state can be found in that basis state, i.e.

$$\langle\psi_d|\,\hat{\rho}\,|\psi_d\rangle = \sum_g \langle\psi_d|\,(|\psi_g\rangle\, p_g\, \langle\psi_g|)\,|\psi_d\rangle = p_g \delta_{gd}. \tag{2.3}$$

It is also worth noting that since kets can be represented as complex vectors in the Hilbert space, state density operators can be described as matrices of probabilities for different states. The diagonal, $|\psi_d\rangle\langle\psi_d|$, of this matrix describes the probability of different states in a chosen basis and the possible off-diagonal values, $|\psi_d\rangle\langle\psi_g|$, emerge if the state our matrix is describing is a coherent superposition of the basis states. [19, app. A]. Hence, we can also calculate a density matrix for pure states in which case the equation simplifies to $\hat{\rho} = |\Psi\rangle\langle\Psi|$. We can distinguish pure and mixed states from each other by taking the trace of the squared density matrix resulting in [19, app. A]

$$\begin{aligned} \mathrm{Tr}\,\hat{\rho}^2 &= 1, \text{for pure states} \\ 0 < \mathrm{Tr}\,\hat{\rho}^2 &< 1, \text{for mixed states.} \end{aligned} \tag{2.4}$$

One descriptive way to visualize any pure or mixed state of a two-dimensional Hilbert space is through the Bloch sphere. For polarization, this sphere is similar to the Poincaré sphere. In the Bloch sphere, any state can be represented by a vector. For example, any coherent superposition state can be described by a so-called Bloch-vector which reaches from the origin on to the surface of this Bloch sphere. In figure 2.1 we have an example of a Bloch sphere for the two-dimensional polarization state space. In the sphere, the coherent superpositions can be described with the equation

$$|\Psi\rangle = \cos\left(\frac{\theta}{2}\right) e^{-i\varphi/2}\,|H\rangle + \sin\left(\frac{\theta}{2}\right) e^{i\varphi/2}\,|V\rangle\,, \tag{2.5}$$

where θ is the azimuthal angle on the $|H\rangle\,|V\rangle$,$|D\rangle\,|A\rangle$ plane and φ is the inclination angle. Hence, the normalized complex coefficients can be changed to any allowed value by changing the two angles, i.e. $\theta \in [0, 2\pi]$ and $\varphi \in [0, \pi]$. The difference between a mixed state and a pure state can be seen from the length of the Bloch-vector. Similarly to the definition in equation (2.4), if the Bloch-vector length is smaller than unity, i.e. it's not on the spheres surface, it is a mixed state. The three different coefficients of the Bloch-vector are defined by the values we get by projecting the state onto all three axis directions of the Bloch sphere. For our two-dimensional states the projections correspond to the Pauli-matrices

$$\sigma_1 = \begin{bmatrix} 0 & 1 \\ 1 & 0 \end{bmatrix}, \quad \sigma_2 = \begin{bmatrix} 0 & -i \\ i & 0 \end{bmatrix} \quad \text{and} \quad \sigma_3 = \begin{bmatrix} 1 & 0 \\ 0 & -1 \end{bmatrix}. \tag{2.6}$$

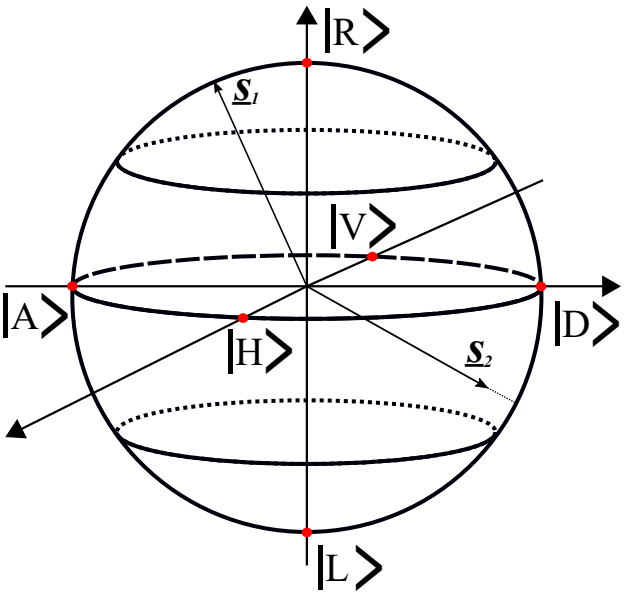

Figure 2.1. *The Bloch sphere for the polarization states of light. A set of three mutually unbiased bases (MUBs) for polarization are shown. These are horizontal; vertical (H,V), anti-diagonal; diagonal (A,D) and left-; right-circular (L,R). Bloch-vector* $\underline{\mathbf{s}_1}$ *describes a coherent superposition state that can be expressed as a superposition in any of the three bases. Conversely, the Bloch-vector* $\underline{\mathbf{s}_2}$ *describes a mixed state since it's length isn't unity, i.e. it doesn't reach the surface of the sphere.*

Using these matrices, the Bloch-vector is defined as

$$\hat{\rho} = \frac{1}{2}(I_2 + \underline{\mathbf{s}} \cdot \sigma), \tag{2.7}$$

where I_2 is the two dimensional identity matrix, $\sigma^2 = \sigma_1^2 + \sigma_2^2 + \sigma_3^2$ and the Bloch-vector $\underline{\mathbf{s}} = [s_1, s_2, s_3]$ [19, app. A]. The Bloch sphere also visualizes how a state is projected onto a basis when it is measured, i.e. if measuring in the $|H\rangle, |V\rangle$-basis, the measured states Bloch vector is projected onto the $|H\rangle, |V\rangle$-axis and the result ($|H\rangle$ or $|V\rangle$) depends probabilistically on how close or far away the projected vector is from either surface of the sphere. Meaning that, if e.g. the projection ends up as a zero vector in the origin, both states ($|H\rangle$ or $|V\rangle$) are equally probable results. More specifically, projections onto a state $|\psi_i\rangle$ are represented by a projection operator $|\psi_i\rangle\langle\psi_i|$. Hence, if our state $|\psi_i\rangle$ is a part of an orthogonal complete set of states $\{|\psi_j\rangle$; j is an integer$\}$, then projecting the pure state $|\Psi\rangle$ onto it works with a probability

$$P_{\psi_i} = \langle\Psi|\psi_i\rangle\langle\psi_i|\Psi\rangle = |c_i|^2. \tag{2.8}$$

Here, c_i is the specific complex coefficient of our state i when expanding the state $|\Psi\rangle$ as a super-

position of the states $\{|\psi_j\rangle\}$, i.e.

$$|\Psi\rangle = \sum_j c_j |\psi_j\rangle = \sum_j |\psi_j\rangle \langle\psi_j|\Psi\rangle . \tag{2.9}$$

As an example of a projection, if our orthogonal basis is $|H\rangle, |V\rangle$ and we project the state $|\Psi\rangle = \frac{1}{\sqrt{3}}|H\rangle + \sqrt{\frac{2}{3}}|V\rangle$ onto a $|H\rangle$ state, the projection would end up in the $|H\rangle$ state only with a $\frac{1}{3}$ probability. But after this projective measurement, if we find the system once in $|H\rangle$, we won't find it in the state $|V\rangle$ in a consequent measurement inside this basis. [19, app. B]

The $|H\rangle, |V\rangle$ basis we have been working in, is just one mutually unbiased basis (MUB) out of three, for the two-dimensional polarization. MUBs are defined by the property, that when we prepare a state in one MUB and measure it in a different MUB, the measured state can be any state of the MUB we measure in, i.e. with a probability $\frac{1}{2}$ for both of our two states in a two-dimensional Hilbert space [21]. For example, if we have an anti-diagonally $|A\rangle$ polarized state and we measure it in the $|H\rangle, |V\rangle$ basis, we get either $|H\rangle$ or $|V\rangle$ with a 50% change for each. Hence, the $|H\rangle, |V\rangle$ and the anti-diagonal diagonal basis ($|A\rangle, |D\rangle$) are mutually unbiased. The third and final mutually unbiased basis to our set of polarization MUBs, is the circular polarizations $|R\rangle$ and $|L\rangle$, that are also displayed in figure 2.1. When placing these different MUBs into our two-dimensional Bloch-sphere, a basis corresponds to a line or an axis travelling through the center of the sphere. Then the MUBs to this one axis are all its orthogonal axes in the Bloch-sphere. Thus, the Bloch-vector coefficients correspond to the state's projections in three different MUBs. We should then be able to relate all the projecting Pauli matrices to the three different MUBs. If we work in the $|H\rangle, |V\rangle$-basis (first dimension of our vectors is $|H\rangle$ and the second one is $|V\rangle$), σ_1 corresponds to the $|A\rangle, |D\rangle$-basis projection, σ_2 corresponds to the $|R\rangle, |L\rangle$-basis projection and σ_3 to the $|H\rangle, |V\rangle$-basis. Note, that even though we've only discussed the two-dimensional case here, the same concepts apply to higher-dimensional state spaces. For higher-dimensional state spaces the number of MUBs is known to be d+1 for state spaces of dimensionality d, if d is a power of prime number [21]. Also, for state projections done across MUBs we get successful measurement with the probabilities $\frac{1}{d}$ instead of $\frac{1}{2}$.

Finally, now that we have discussed the fundamentals of discrete quantum states, we will introduce some basic concepts about state transformations. The important concept when it comes to state transformations is unitarity. Unitary transformations are transformations that change a certain degree of freedom of the system without extracting any energy out of the system or changing the orthogonality of two states modulated by this transformation [22, ch.4]. What this orthogonality condition specifically means is that if two states are operated on by the same unitary transformation, the inner product of the states stays the same. One example of a device with a non-unitary operation is the polarizer that absorbs the portion of photons that are in an orthogonal polarization state or that are randomly projected to an orthogonal state from a superposition. For example, in this operation the inner product of a $|D\rangle$ and a $|H\rangle$ state doesn't remain the same, since either system the states describe can be absorbed by the polarizer, and if they transmit through the polarizer they have the same polarization state afterwards. In contrast, one example of a unitary transformation is a Half-Wave Plate (HWP) that rotates the linear polarization of a photon. This means that, for example, a diagonal polarization can be rotated according to $\hat{U}_{HWP}|D\rangle = |A\rangle$ when operated

on by the unitary transformation operator of a HWP. The unitary transformations are usually described by a unitary operation matrix $\hat{U}$. In the following example the computational basis of the matrix is chosen to be the $|H\rangle, |V\rangle$ basis. Thus, we can use the following simple vector notations for the states

$$|H\rangle = \begin{bmatrix} 1 \\ 0 \end{bmatrix}, \quad |V\rangle = \begin{bmatrix} 0 \\ 1 \end{bmatrix}, \quad |D\rangle = \frac{1}{\sqrt{2}} \begin{bmatrix} 1 \\ 1 \end{bmatrix} \quad \text{and} \quad |A\rangle = \frac{1}{\sqrt{2}} \begin{bmatrix} 1 \\ -1 \end{bmatrix} \tag{2.10}$$

The unitary matrix for a HWP, oriented to turn $|D\rangle$ polarization into $|A\rangle$ polarization is quite simple to understand in this polarization Hilbert space, and it is of the form

$$\hat{U}_{HWP} = \begin{bmatrix} 1 & 0 \\ 0 & -1 \end{bmatrix}. \tag{2.11}$$

From this example it can also be seen that the orthogonality between $|D\rangle$ and $|A\rangle$ would be conserved if both are operated on by this unitary. The same holds for the $|H\rangle$ and $|V\rangle$ states that only get a possible phase term in the HWP, if the HWP is oriented to shift $|D\rangle$ and $|A\rangle$ polarizations.

2.1.2 Quantized electro-magnetic waves

Now we move on from describing more abstract states to describing physical ones, i.e. quantum states of light. The quantum mechanical theory of light and photons consists of describing quantized excitation of the electro-magnetic field modes. But due to the topics of this thesis, we skip most of this background and only pick out concepts and results from this theory, that are useful in our applications.

The quantization of the electro-magnetic (EM) field can be achieved by treating the EM-field as harmonic oscillators, with varying frequencies, polarizations, spatial positions etc., and confining this field into a finite box. We also add the boundary condition that the field vanishes at the box boundaries. In this quantization of the harmonically oscillating EM-field, we can describe each mode of the field with its own non-Hermitian operator pair $\hat{a}$ and $\hat{a}^\dagger$. If we choose the relations between these two non-commuting operators correctly, we will arrive at a familiar form of the quantized harmonically oscillating field Hamiltonian

$$H = \hbar\omega \left(\hat{a}^\dagger \hat{a} + \frac{1}{2} \right), \tag{2.12}$$

where the equation resembles the eigenvalues of a regular quantized harmonic oscillator but with the introduction of the combined operator $\hat{a}^\dagger \hat{a}$ [20]. The eigenstates of this equation are called number states or Fock-states $|n\rangle$, and they basically describe how many quanta n of energy, i.e. photons, this one harmonically oscillating field mode with angular frequency ω has. To reiterate, one of these Fock-states only describes the number of light quanta that exist in this one harmonically oscillating field mode with a certain set of values for its degrees of freedom, i.e. a certain polarization, spatial structure and so on. The combined operator $\hat{a}^\dagger \hat{a}$ is often called the number

operator $\hat{n}$, and the eigenstates of this Hamiltonian fulfill the equation

$$H|n\rangle = \hbar\omega\left(\hat{n}+\frac{1}{2}\right)|n\rangle = \left(n+\frac{1}{2}\right)\hbar\omega|n\rangle. \tag{2.13}$$

Here n is the number of energy quanta that are in the eigenstate $|n\rangle$, and as could be expected, the energy a single photon adds to the field is $\hbar\omega$. Interestingly, this harmonic oscillator Hamiltonian also gives a zero point energy of $\hbar\omega/2$ to the vacuum state $|0\rangle$. This phenomenon is purely a quantum one and spontaneous processes, like spontaneous emission of light, are commonly thought to be stimulated by these zero-point fluctuations of the EM-field. [19, ch.2-4]

In addition to forming the photon number operator $\hat{n}$, the creation operator $\hat{a}^\dagger$ and annihilation operator $\hat{a}$ have their separate uses in quantum mechanical theory. As the names of these operators indicate, they can create and remove a quantum of energy from the Fock-states, such that

$$\begin{aligned}\hat{a}|n\rangle &= \sqrt{n}|n-1\rangle \\ \hat{a}^\dagger|n\rangle &= \sqrt{n+1}|n+1\rangle.\end{aligned} \tag{2.14}$$

Hence, in any quantum mechanical model that includes photon absorption or creation, these operators are included. Also, these two relations do require a lower limit since the energy of a quantized harmonic oscillator can't be zero or negative. This is done by introducing a lower bound to the annihilation operator $\hat{a}|0\rangle = 0$, that can be thought to naturally occur due to the multiplier $\sqrt{n} = \sqrt{0}$ caused by equation (2.14). An important thing to note is the fact that these annihilation and creation operators only describe the changes in numbers of energy quanta in one specific EM-field mode, i.e. Fock -state. Then, similarly to the Fock-states, these operators only operate on a specific mode of the EM-field. This can be also interpreted as the individual excitations or photons having these same properties as the EM-field mode. [19, ch.2]

Next, we need to connect the actual harmonic EM-field to these excitations or photons. Since the annihilation and creation operators were initially introduced when deriving the quantization of these harmonic fields, the operators for these fields can be stated using these two operators. Hence, we have a general form of the electric and magnetic field components for multiple different wave vectors and polarizations of light

$$\begin{aligned}\hat{\underline{\mathbf{E}}}(\underline{\mathbf{r}},t) &= i\sum_{\underline{\mathbf{k}},s}\left(\frac{\hbar\omega_k}{2\varepsilon_0 V}\right)^{\frac{1}{2}}\hat{\underline{\mathbf{e}}}_{\underline{\mathbf{k}},s}\left[\hat{a}_{\underline{\mathbf{k}},s}e^{i(\underline{\mathbf{k}}\cdot\underline{\mathbf{r}}-\omega_k t)} - \hat{a}^\dagger_{\underline{\mathbf{k}},s}e^{-i(\underline{\mathbf{k}}\cdot\underline{\mathbf{r}}-\omega_k t)}\right], \\ \hat{\underline{\mathbf{B}}}(\underline{\mathbf{r}},t) &= \frac{i}{c}\sum_{\underline{\mathbf{k}},s}(\hat{\underline{\mathbf{k}}}\times\hat{\underline{\mathbf{e}}}_{\underline{\mathbf{k}},s})\left(\frac{\hbar\omega_k}{2\varepsilon_0 V}\right)^{\frac{1}{2}}\left[\hat{a}_{\underline{\mathbf{k}},s}e^{i(\underline{\mathbf{k}}\cdot\underline{\mathbf{r}}-\omega_k t)} - \hat{a}^\dagger_{\underline{\mathbf{k}},s}e^{-i(\underline{\mathbf{k}}\cdot\underline{\mathbf{r}}-\omega_k t)}\right],\end{aligned} \tag{2.15}$$

where ε_0 is the vacuum permittivity, $\hat{\underline{\mathbf{e}}}_{\underline{\mathbf{k}},s}$ are the different polarization unit vectors for wave vectors $\underline{\mathbf{k}}$ and polarization directions s, ω_k are the angular frequencies corresponding to each wave number, $\hat{\underline{\mathbf{k}}}$ is a unit vector in the wave vector direction, c is the speed of light, t is time, $\underline{\mathbf{r}}$ is position, and V is the box volume that confines the fields. Here the creation and annihilation operators are explicitly related to modes with a specific $\underline{\mathbf{k}}$-vector and polarization. The box volume is introduced due to the boundary conditions that are designed to circumvent some infinities of an infinite vacuum. But

the boundary distances can be set to infinity after any calculations to achieve physical results. This should be done since all results are supposed to be independent of the initial box size, unless we are actually working in a finite box. [19, ch.2]

One extra notation often used, is called the negative and positive frequency parts of the field operators and they are defined as

$$\begin{aligned}\hat{\underline{\mathbf{E}}}(\underline{\mathbf{r}},t) =& \hat{\underline{\mathbf{E}}}^{(+)}(\underline{\mathbf{r}},t) + \hat{\underline{\mathbf{E}}}^{(-)}(\underline{\mathbf{r}},t),\\ \hat{\underline{\mathbf{E}}}^{(+)}(\underline{\mathbf{r}},t) =& i\sum_{\underline{\mathbf{k}},s}\left(\frac{\hbar\omega_k}{2\varepsilon_0 V}\right)^{\frac{1}{2}} \hat{\underline{\mathbf{e}}}_{\underline{\mathbf{k}},s}\hat{a}_{\underline{\mathbf{k}},s}e^{i(\underline{\mathbf{k}}\cdot\underline{\mathbf{r}}-\omega_k t)},\\ \hat{\underline{\mathbf{E}}}^{(-)}(\underline{\mathbf{r}},t) =& \left[\hat{\underline{\mathbf{E}}}^{(+)}(\underline{\mathbf{r}},t)\right]^{\dagger},\end{aligned} \tag{2.16}$$

for the electric field and similarly for the magnetic field. However, since the magnetic field is, relatively, weaker compared to the electric field, and isn't as important in light-matter interactions, the electric field is what we will mainly focus on when describing light fields. [19, ch.2]

Thus far we have only introduced one type of state of light, the so-called Fock-states which can be used to express other, more classical types of light. Constructing other states of light using the Fock-states is also useful when trying to understand the differences between different types of light. The most sensible place to start is of course thermal light, since that is the type of light coming out of a radiating black body, and approximately the type of light we get from the sun. The monochromatic mixture of different number states, that is a thermal light state, can be derived from the Planck distribution and is of the form [19, ch.2]

$$\hat{\rho} = \frac{1}{1+\overline{n}}\sum_{n=0}^{\infty}\left(\frac{\overline{n}}{1+\overline{n}}\right)^n |n\rangle\langle n|, \tag{2.17}$$

where $\overline{n}$ is the average photon number for the specific field mode and $|n\rangle$ are the possible number states the thermal field contains. When comparing equation (2.17) to equation (2.2), we can see that thermal light is a incoherent mixture of different Fock-states. Another important state of light is the coherent state, usually connected to laser light. This coherent state $|\alpha\rangle$ is defined as a coherent superposition of number states [19, ch.3]

$$|\alpha\rangle = \exp\left(-\frac{1}{2}|\alpha|^2\right)\sum_{n=0}^{\infty}\frac{\alpha^n}{\sqrt{n!}}|n\rangle, \tag{2.18}$$

where the coefficients of the monochromatic number states obey a Poissonian distribution around the average $\overline{n} = |\alpha|^2$. The coherent states are also eigenstates of the annihilation operator such that

$$\hat{a}|\alpha\rangle = \alpha|\alpha\rangle. \tag{2.19}$$

For our applications, the main reason why it is important to draw distinctions between these different states of light is the fact that they differ in their so-called photon statistics. These statistics measure the detection probabilities of photons in a certain state of light during a short time interval. The two important characteristics then are the average number of photons detected in this

time interval over multiple measurements and the standard deviation of these statistics. For coherent light states these two values follow a Poissonian distribution, meaning that the variance of the detected photon numbers in a certain time interval is equal to the average number of detections over the repeated measurements [23]. Then the arrival frequencies of photons in a coherent state are random, since Poissonian distributions describe random processes with a binary result. For example, radioactive decay also follows the same statistic. In contrast, Fock-states follow sub-poissonian statistics, which means that the variance in the photon detections is smaller than the average number of photons detected in a time interval, i.e. $\Delta n^2 < \overline{n}$ if we use the same variables as in equation (2.17). In this regime, with a decreasing variation we get an increasingly regular interval between the detected photons [24]. For us, these regular intervals are the most desirable property of Fock-states and also the main reason why we can use single photon Fock-states in secure quantum communication applications like cryptography introduced in section 4.1. In short, this property just means that, when sending multiple single photons e.g. in a communication scheme, we have an ideally zero probability of two photons temporally overlapping. If this property didn't exist, the security of our single photon communication schemes would be compromised since an eavesdropper could extract the information out of only one of the two overlapping photons without us noticing.

2.2 Nonlinear optical interactions

Now that we have introduced single photon states, we need a method to efficiently produce them, e.g. in our case with heralded single photons. These heralded single photons are just photon pairs in which one photon is used as a trigger for signaling when the other half of the pair was generated. Thus, the second photon can be used as a perfect single photon state when we just compare its timing to its heralding counterpart. This heralding needs to be done since it ensures that our photons are in a single photon Fock-state [25]. With these heralded single photons, the way we know that we are detecting our single photon state is by the time correlation with its heralding partner photo, i.e. the two are created roughly at the same time. In this section we will describe the nonlinear light-matter interactions that can be used in creating these photon pairs. This section follows mostly R. Boyd's book [26] on nonlinear interactions. Again, for a more complete description of nonlinear light-matter interactions we refer to literature, like the aforementioned book.

In the Lorentz model, when a material is subject to the oscillating electric field of light, the material can absorb the photons if the frequency of the EM-field is close to the natural resonance frequency of the material [27, ch.3]. Or the material can be polarized by the electric field if the frequency isn't close to this resonance frequency. These oscillators in the material, that the field can polarize, are described by the Lorentz model as the outer electrons and the corresponding shielded core acting as a dipole that can oscillate in an external field. The material polarization is defined as the materials dipole moment per unit volume. When we include a nonlinear term into the restoring forces of these oscillating dipole's equations of motion. We get a nonlinear response in the material polarization when an external electric field is interacting with the material. If the material has

these nonlinear responses, the simplified scalar version of material polarization follows roughly the equation

$$P(t) = \chi^{(1)}E(t) + \chi^{(2)}E^2(t) + \chi^{(3)}E^3(t) + ..., \tag{2.20}$$

where the quantities $\chi^{(i)}$ are the nonlinear susceptibility values defining the strength of the materials linear (when $i = 1$) and nonlinear responses ($i > 1$). For vector fields these susceptibilities become tensors. In the above equation the input electric field can be composed of multiple different frequency components, e.g. if we now move back to vector fields

$$\underline{\mathbf{E}}(t) = \underline{\mathbf{E_1}}\exp(-i\omega_1 t) + \underline{\mathbf{E_2}}\exp(-i\omega_2 t) + c.c., \tag{2.21}$$

where $c.c.$ denotes the complex conjugate of the previous terms. This then can result in nonlinear material polarization responses that oscillate, e.g. with a frequency that is the sum or difference of these two electric field frequencies. These two examples correspond to phenomena called sum frequency generation and difference frequency generation. The different susceptibility tensor values, e.g. $\chi^{(2)}_{ijk}(\omega_3, \omega_2, \omega_1)$, of a material tell the efficiency of these different nonlinear material responses, for specific field polarizations. The specific values of these tensors depend on the frequencies of the mixing electric fields and material polarization, along with the polarization directions of all of these components. Hence, usually when these phenomena are used, the crystal properties are tuned in such a way that only a specific nonlinear frequency component is produced efficiently. [26, ch.1]

In this thesis we only focus on the second order nonlinearity, i.e. $\chi^{(2)}$ related effects. One example of these effects is difference frequency generation where the local material polarization oscillates at a frequency that is the difference of 2 different input fields

$$P^{(2)}_i(t) = \sum_{jk} \chi^{(2)}_{ijk}(\omega_1 - \omega_2, \omega_1, \omega_2)\left[E_{1,j}E_{2,k}e^{-i(\omega_1-\omega_2)t} + c.c.\right], \tag{2.22}$$

where $\chi^{(2)}_{ijk}$ is a specific component of the second-order susceptibility tensor, E_j and E_k are the input electric fields and the indices ijk define specific cartesian directions, i.e. polarization directions of the fields and the material. The utilizability of these nonlinear responses comes from the fact that a regularly oscillating material polarization can induce an EM-field. Effectively creating light with a different frequency compared to the input field or fields. These effects are then used in tuning laser frequencies and even in creating photon pairs as we will demonstrate in the next section [28]. The way an EM-field is created by nonlinear material polarization responses can be seen from the wave equation of light in a nonlinear medium. When deriving this wave equation, the only difference in comparison to the free-space equation is that now the electric flux density is described by $\underline{\mathbf{D}}_n = \underline{\mathbf{E}}_n + 4\pi\underline{\mathbf{P}}^{(1)}_n + 4\pi\underline{\mathbf{P}}^{NL}_n$, where the second to last term is the linear polarization response of the medium and the last term is the nonlinear response. The liner response can be described with the more common notation $\underline{\mathbf{E}}_n + 4\pi\underline{\mathbf{P}}^{(1)}_n = \underline{\varepsilon}^{(1)}_r(\omega_n)\cdot\underline{\mathbf{E}}_n$, where $\underline{\varepsilon}^{(1)}_r(\omega_n)$ is the wavelength dependent dielectric vector. If the material is assumed to be nonmagnetic, free of

current and absent of free charges we can use Maxwell's equations to derive the wave equation

$$\nabla \times \nabla \times \underline{\mathbf{E}}_n + \frac{\underline{\varepsilon}_r^{(1)}(\omega_n)}{c^2} \cdot \frac{\partial^2 \underline{\mathbf{E}}_n}{\partial t^2} = \frac{-4\pi}{c^2} \frac{\partial^2 \underline{\mathbf{P}}_n^{NL}}{\partial t^2}, \tag{2.23}$$

for a specific frequency $\omega_n > 0$. If our incident electric fields induce an oscillating nonlinear polarization response $\underline{\mathbf{P}}_n^{NL}(\underline{\mathbf{r}},t) = \underline{\mathbf{P}}_n'^{NL}(\underline{\mathbf{r}}) \exp(-i\omega_n t) + c.c.$ the right hand side of equation (2.23) is non-zero. This can be interpreted as the nonlinear response acting like a source for the electric field $\underline{\mathbf{E}}_n$. [26, ch.1-2]

We will now go back to our examples of sum and difference frequency generation (SFG and DFG). With the concepts and equations listed above, if we have a nonlinear material with a response described by the frequency and polarization dependent tensor value $\chi_{ijk}^{(2)}(\omega_3, \omega_1, \omega_2)$, we can produce a light field of frequency ω_3 by having two light fields ω_2 and ω_1 incident on our nonlinear material. These processes are called parametric, and one characteristic of parametric processes is that the input and output photons have the same total energy. For SFG, this simply means that $\hbar\omega_3 = \hbar\omega_2 + \hbar\omega_1$, if ω_1 and ω_2 are the incident photon frequencies. But for DFG, the single photon picture is a bit more complicated since the incident fields have higher energy than the induced field $\omega_3 = \omega_1 - \omega_2$. In the single photon picture, this means that the higher energy ω_1 photon is absorbed and the ω_2 photon stimulates the emission of another ω_2 photon. Since the process is parametric, this means that the remaining absorbed energy is emitted in the form of a photon with energy $\hbar\omega_3 = \hbar\omega_2 - \hbar\omega_1$, i.e. two photons are emitted in the process. For our experiments, the important special case is when we remove the second incident field ω_2 and the two photons are spontaneously excited. [26, ch.1]

2.2.1 Spontaneous parametric down-conversion

In this thesis we only utilize this spontaneous version of DFG called spontaneous parametric down-conversion (SPDC). In SPDC, a single high energy field excites two photons, which energies sum up to the initial pump photon energy. This is visualized in figure 2.2, where it's also shown that only a part of the pump light of angular frequency ω_p is converted into the signal and idler photons of frequencies ω_s and ω_i. Even though in figure 2.2 the signal and idler beams seem to be of the same frequency, they can differ as long as they fulfill the energy conservation of a parametric process, i.e. $\omega_p = \omega_i + \omega_s$.

Since we are looking at the two photon emission of SPDC, it is useful to examine it on a single photon level. We can start with a continuous input of pump photons ω_p incident onto a nonlinear crystal. Then with a probability proportional to a specific component $\chi_{ijk}^{(2)}$ of the crystals second order susceptibility, a portion of the pump photons are converted into two single photons of the frequency ω_s and ω_i. Under a quantum mechanical examination of the process we end up with an output state that can be described as [29, 30, 31]

$$|\Psi_{out}\rangle = |vac\rangle + \int d\underline{\mathbf{k}}_s \int d\underline{\mathbf{k}}_i \Phi(\underline{\mathbf{k}}_s, \underline{\mathbf{k}}_i) \left| 1_{\underline{\mathbf{k}}_s}, 1_{\underline{\mathbf{k}}_i} \right\rangle, \tag{2.24}$$

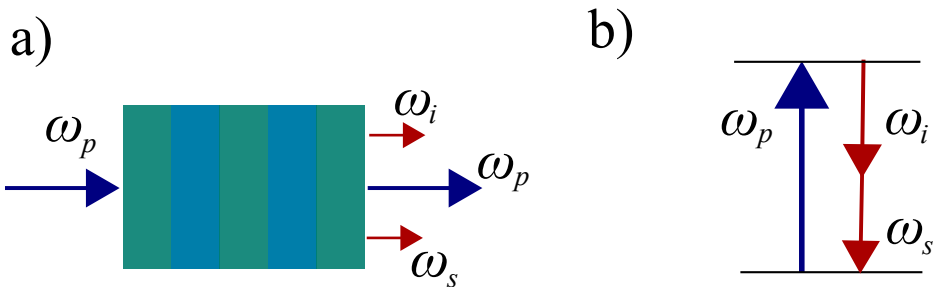

Figure 2.2. *Diagrams representing spontaneous parametric down-conversion. In a) the striped block represents our nonlinear crystal and by pumping it with a wavelength of ω_p, we can spontaneously excite two photons with frequencies ω_i and ω_s. Since the process is parametric, the energy of the input pump photon should be the same as the sum of the 2 output photons as shown in the virtual energy level description in b).*

where $|vac\rangle$ is the initial vacuum state and $\Phi(\underline{\mathbf{k}}_s, \underline{\mathbf{k}}_i)$ is the so-called two-photon amplitude (TPA) of the two-photon Fock-state $\left|1_{\underline{\mathbf{k}}_s}, 1_{\underline{\mathbf{k}}_i}\right\rangle = \left|1_{\underline{\mathbf{k}}_s}\right\rangle \left|1_{\underline{\mathbf{k}}_i}\right\rangle$. The TPA includes properties like the pump spectrum, and nonlinear susceptibility, along with the phase-matching condition and energy conservation. As a result, the TPA can be used to determine the spectral or momentum distributions of the signal and idler photons created in the nonlinear interaction. For our use cases controlling both the spectral and spatial properties of the photons are important. We can create most of the wanted changes in the TPA e.g. by changing the bandwidth of the pump laser, by spatial and spectral filtering after the pair has been created, and by changing the parameters related to the phase-matching of the process, which we will discuss next [30, 32].

2.2.2 Phase-matching

Since nonlinear phenomena are not very strong [26, 33], in order to make use of them, the nonlinear crystal parameters are tuned for the wanted nonlinear phenomenon to work efficiently. One of the more important parameters affecting the efficiency, and indirectly the output wavelengths of a nonlinear process, is phase-matching.

Phase-matching is a condition that keeps the phase of the induced material polarization and the generated light wave fixed through the material. This can be also thought of as the individual dipole oscillators emitting light with a correct phase relation for the individual emitted fields to add to the fields emitted by other oscillators [26, ch.2]. The fulfillment of this condition increases the achievable gain in the generated field. Meaning that perfect phase-matching, i.e. $\Delta k = \sum_i k_{out,i} - \sum_j k_{in,j} = 0$ in a collinear system, results in a sharp increase in the nonlinear process efficiency. Hence, in the single photon picture of a parametric process, this can be described as a momentum conservation between the input pump photon and the output photons it is converted into [34]. One example is the effect of phase-matching on the efficiency of second harmonic generation (SHG),

which is a second order nonlinear phenomenon where we have one input incident field frequency and an output frequency that is twice the input frequency. If we examine the SHG response of a material by using a theoretical nondepleting plane wave pump, the output power scales as [26, 35]

$$I_{SHG} \propto L^2 \operatorname{sinc}^2\left(\frac{\Delta kL}{2}\right), \tag{2.25}$$

where L is the crystal length, or the length of the interaction region. From this equation it can be seen that if we don't have perfect phase-matching, the power in the output field will starts flowing back to the input field after a certain crystal length. This happens when the output field in the crystal starts getting out of phase with the material polarization driving it, and the length after which this decrease starts is sometimes defined as the phase-matching coherence length $l_c = \pi/\Delta k$ [35]. Note, that we use SHG as an example of a second order nonlinear process because of its simplicity and the wide array of literature focusing on it. Similar phase-matching conditions to the one in equation (2.25) can be found for SPDC [29, 36].

As an example, in collinear SPDC (i.e. input and output light propagate collinearly) the wave vector difference is of the form $\Delta k = k_i + k_s - k_p \Leftrightarrow n_i\omega_i + n_s\omega_s = n_p\omega_p$. This means that in the degenerate case $\omega_i = \omega_s = 1/2\omega_p$, the phase-matching would require the refractive index inside the material to be $n(2\omega) = n(\omega)$, which isn't the case in materials with normal dispersion [26, ch.2]. Because of this restriction, most crystals used in nonlinear processes also exhibit birefringence. In simple terms this entails that the refractive index inside the crystal depends on the polarization of the light, in addition to the material dispersion. In the commonly used uniaxially birefringent crystals, the crystal has a crystal axis called the optic axis. Any light polarized along the plane formed by this optic axis and the lights wave vector experiences a material dependent extraordinary refractive index n_E, and light polarized perpendicular to this plane experiences the ordinary refractive index n_o [26, ch.2]. If the polarization is in an angle between these two polarization directions described above, the refractive index felt by the light field will be between the two extrema n_E and n_o. Because of this polarization dependent refractive index, it is possible to achieve this collinear phase-matching by choosing your nonlinear material in a way that allows us to take advantage of the birefringence. In phase-matched nonlinear processes involving three light fields, if the two lower energy light fields have different polarizations, the process is called a type 2 phase-matched process. Similarly, if the polarizations are the same for these two fields but different from the higher energy fields polarization, the process is called a type 1 process. If all the polarizations are identical, the process is usually referred to as a type 0 process. But in these type 0 processes the phase-matching is achieved by different methods [37].

Since we can also achieve different refractive indices between n_E and n_o by varying the polarizations angle in relation to the optic-axis, we can adjust the phase-matching by changing the incidence angles of the fields into the material. In a birefringent material however, this can result in beam walk-off between the orthogonal polarizations and result in non-collinear operation. In contrast, for collinear operation in some crystals, a better way to fine tune phase-matching is via the temperature dependence of the birefringent refractive indices. [26, ch.2]

Quasi-phase-matching

Finally, the phase-matching solution used in this thesis is called quasi-phase-matching (QPM). The operating principle of this phase-matching method comes from the fact that, as can be seen in equation (2.25) for SHG, the acquired power in nonlinear processes depends on the length of the interaction region if $\Delta k \neq 0$. The idea behind QPM is that we could compensate for the

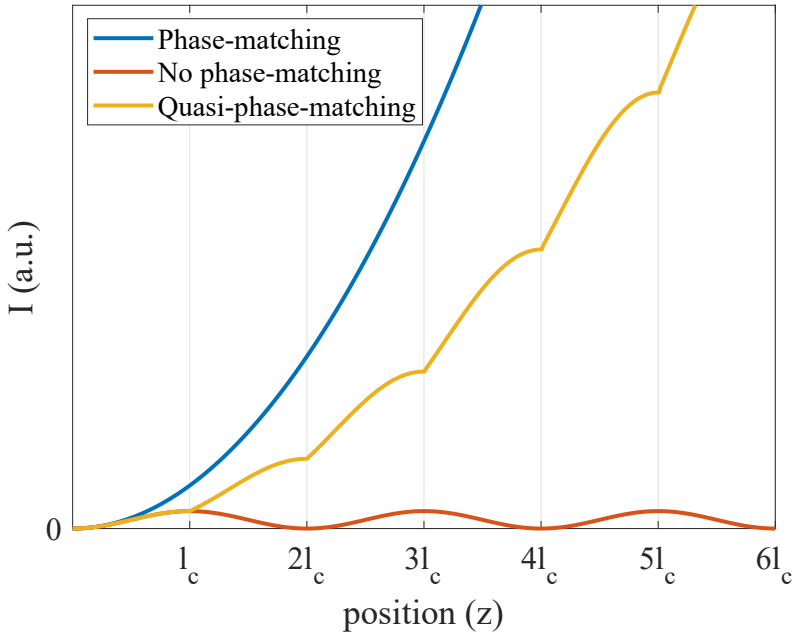

Figure 2.3. *A figure representing the crystal length dependent nonlinear output intensity for a perfectly phase-matched case, a quasi-phase-matched case and a no phase-matching case. The curves are plotted using the equations (2.25 and 2.26) for SHG, but they give a rough picture of quasi-phase-matching for all parametric second order nonlinear phenomena. The value l_c is the so-called a coherence length for a phase mismatch. The figure is based on the similar figure in [35].*

phase mismatch between the driving material polarization and the generated field by periodically changing the crystal structure [35]. One way this could be done is by flipping the crystal structure periodically, and hence periodically changing the effective nonlinear susceptibility. We would then periodically compensate for the relative phase shift that happens between the material polarization and the output fields [35]. This can be easily seen from the interaction region length dependence for SHG's output electric field amplitude

$$\frac{dE_{SHG}}{dz} = \frac{i\omega E_p^2}{2n_{SHG}c} d(z) \exp(-i\Delta k z) \tag{2.26}$$

where E_p is the pump field amplitude, ω is the pump frequency and n_{SHG} is the refractive index of the material felt by the SHG field [35]. A few of the key approximations here are losslessness, collinearity of the input and output light, and a continuous-wave pump field. In this equation $d(z)$ is the periodically changing nonlinear susceptibility coefficient. In the optimal case, whenever $\exp(-i\Delta k z)$ changes the right side of equation (2.26) into negative real values, i.e. the field gain

starts turning into loss, $d(z)$ should change sign between $\pm\chi^{(2)}_{eff}$. This changing of the effective susceptibility $\chi^{(2)}_{eff}$ could, for example, correspond to multiple layers of the nonlinear crystal with the adjacent layers rotated by 180° [35]. Thus, the real part of equation (2.26) can be kept positive for the whole crystal length, even when $\Delta k \neq 0$. Hence, we can achieve continuous gain in the whole length of the crystal. These periodic poling change between $\pm\chi^{(2)}_{eff}$ can be derived into an effective collinear wave vector mismatch in QPM materials

$$\Delta k' = k_i + k_s - k_p + \frac{2\pi}{\Lambda}, \tag{2.27}$$

where Λ is the QPM poling period [34, 35]. Meaning that quasi-phase-matching can be achieved when $\Delta k' = 0$. But even though QPM can greatly increase the power achieved when the wave vectors are mismatched, the achieved power is still slightly lower compared to nonlinear processes with perfect phase-matching, e.g. by a factor of $2/m\pi$ for SHG [35]. This difference in power can be seen from the plot in figure 2.3.

As before, nonlinear crystal temperature can be used for fine tuning the phase-matching since the refractive indices and the poling period will change with the temperature. This change in the poling period is caused by thermal expansion of the material. [38]

This same phase-matching method works with the collinear SPDC we will be using here. However, one major difference to the shown SHG case is the scaling of the output power in relation to the crystal length L. In our SPDC setup we perform spatial filtering, and in the presence of this filtering the single photon rates should follow roughly the relation $R_c \propto \sqrt{L}$ for a QPM case [39]. This scaling factor might still differ in experiments with different types of spatial or spectral filtering [29].

2.3 Hong-Ou-Mandel interference

Next, we will be discussing how these two single photons, e.g. generated through SPDC, can be used in a two-photon interference phenomenon called Hong-Ou-Mandel (HOM) interference. HOM interference usually refers to a specific case of two-photon interference in a beamsplitter (BS). The more general theory behind it was described by Hong, Ou and Mandel, along with Ghosh, as a fourth order interference that happens between two photons [40]. What they meant by this was that if you bring the two photons, e.g. generated through SPDC, together they exhibit no interference pattern when looking at the detection rate with a single detector at the interference plane (second order interference). But when measuring the spatial correlations between the two overlapped photons, an interference pattern can be observed in the relative separation between them. The interference can be seen in the coincidence rate, or rate of simultaneous detections between two separate detectors. The interference pattern varies cosinusoidally as a function of the separation of the two detectors in the interference plane. Thus, even though the single photon detection rate is almost constant for both detectors, the photon pair interferes with each other and the interference can be seen in the relative distribution of detected photon pairs. They called this a fourth order interference, since the correlation function depends on the product of four field terms.

The common case where this fourth order interference is usually applied is two-photon interference in a beamsplitter. We follow Brańczyk [41] and Hong, Ou, and Mandel [42] in the description of this phenomenon. We can start describing HOM interference in a beamsplitter by using the input and output paths from the beamsplitter. We label the two paths as a, b, as in figure 2.4.

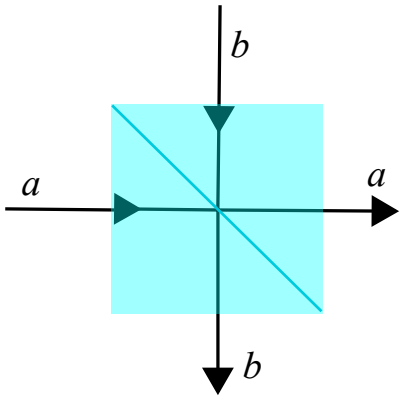

Figure 2.4. *A simple representation of the different photon paths in a beamsplitter.*

Let's assume that we initially have two photons entering the beamsplitter, one from path b and one from path a. We will also assume that the photons enter the beamsplitter at the exact same time. This means that our initial two-photon state can be expressed as $|\Psi_{in}\rangle = \hat{a}^{\dagger}_{a,i}\hat{a}^{\dagger}_{b,j}|vac\rangle = |1\rangle_{a,i}|1\rangle_{b,j}$, where a, b signify the paths and i, j denote the other properties of the photons, i.e. spectral profile, polarization and transverse field structure. The beamsplitter acts on these photon paths as a unitary transformation, if we assume it is lossless. This unitary symmetric beamsplitter can be described in matrix form as

$$\hat{U}_{BS} = \begin{bmatrix} \sqrt{T} & i\sqrt{R} \\ i\sqrt{R} & \sqrt{T} \end{bmatrix}, \tag{2.28}$$

where R is the reflectivity of the beamsplitter and T is the transmittance of the beamsplitter. The two dimensions of this matrix describe the two different paths. This means that the output state of our beamsplitter can be described as

$$\begin{bmatrix} \hat{a}^{\dagger}_{a,out1} \\ \hat{a}^{\dagger}_{b,out2} \end{bmatrix} = \hat{U}_{BS} \begin{bmatrix} \hat{a}^{\dagger}_{a,in1} \\ \hat{a}^{\dagger}_{b,in2} \end{bmatrix}. \tag{2.29}$$

When this unitary acts on our predefined two-photon initial state we get an output

$$\begin{aligned} |\Psi_{out}\rangle &= \hat{U}_{BS}|1\rangle_{a,i}|1\rangle_{b,j} = \hat{U}_{BS}\,\hat{a}^{\dagger}_{a,i}\hat{a}^{\dagger}_{b,j}|vac\rangle \\ &= \left(\sqrt{T}\hat{a}^{\dagger}_{a,i} + i\sqrt{R}\hat{a}^{\dagger}_{b,i}\right)\left(i\sqrt{R}\hat{a}^{\dagger}_{a,j} + \sqrt{T}\hat{a}^{\dagger}_{b,j}\right)|vac\rangle \\ &= \left(i\sqrt{TR}\,\hat{a}^{\dagger}_{a,i}\hat{a}^{\dagger}_{a,j} + i\sqrt{TR}\,\hat{a}^{\dagger}_{b,i}\hat{a}^{\dagger}_{b,j} - R\,\hat{a}^{\dagger}_{b,i}\hat{a}^{\dagger}_{a,j} + T\,\hat{a}^{\dagger}_{a,i}\hat{a}^{\dagger}_{b,j}\right)|vac\rangle. \end{aligned} \tag{2.30}$$

This result doesn't look too significant but, if our two photons are indistinguishable in their other degrees of freedom besides path, we can't distinguish which output photon came from which input path. Hence, the indices i, j become redundant when describing these Fock-states. With

these assumptions our output state takes the form

$$\begin{aligned}|\Psi_{out}\rangle &= \left(i\sqrt{TR}\,\hat{a}_a^{\dagger 2} + i\sqrt{TR}\,\hat{a}_b^{\dagger 2} - R\,\hat{a}_b^{\dagger}\hat{a}_a^{\dagger} + T\,\hat{a}_a^{\dagger}\hat{a}_b^{\dagger}\right)|vac\rangle \\ &= (T-R)\,|1_a,1_b\rangle + i\sqrt{2TR}\,|2_a,0_b\rangle + i\sqrt{2TR}\,|0_a,2_b\rangle\,.\end{aligned} \tag{2.31}$$

The multiplier $\sqrt{2}$ in front of the asymmetric terms comes from the $\sqrt{n+1}$ coefficients introduced when using the creation operator, i.e. as in equation (2.14). From this form we see a pretty simple and interesting interference effect, namely if $T-R$ goes to zero our two input photons only exit the beamsplitter in the same output path. In other words, since it is impossible to distinguish which photon came in from which input path, the photons bunch together when they interfere in the beamsplitter. So, for the most interesting case our beamsplitter should be a 50:50 beamsplitter meaning that $R = T = \frac{1}{2}$. This is the only case with the possibility for perfect bunching, since $R+T = 1$ for a unitary operation.

Now we will inspect the beamsplitter HOM interference more carefully. We will assume our beamsplitter to have the ideal reflectance to transmittance ratio of 50:50. We will also be detecting the photons coming out of both outputs, and only look at events where the two photons go to different paths, i.e. coincidences. The probability for a coincidence is again proportional to a product of four electric field terms and can be written as

$$P_{ab} = K\langle \underline{\mathbf{E_a}}^{(-)}(t)\underline{\mathbf{E_b}}^{(-)}(t)\underline{\mathbf{E_b}}^{(+)}(t)\underline{\mathbf{E_a}}^{(+)}(t)\rangle, \tag{2.32}$$

where $\underline{\mathbf{E_i}}^{(\pm)}$ are the single photon electric field negative and positive frequency parts for the two output paths and K is a constant [42]. In the above equation, the optical path lengths between the BS and both detectors are assumed equal, regardless of path. We will also assume that the photons are created through SPDC and both have an identical Gaussian spectral profile. Additionally, we let the relative arrival time of the photons onto the beamsplitter vary by τ, which makes them distinguishable from each other unless $\tau = 0$. We can thus derive an expression for the rate of coincidence detections from equation (2.32). This relation takes the form

$$P_c \equiv P_{ab} = \frac{1}{2}\left[1 - \exp(-(\Delta\omega\tau)^2)\right], \tag{2.33}$$

where $\Delta\omega$ is the bandwidth of the photon's Gaussian spectral distributions [42]. This gives us a clear τ dependent form of the coincidence counts. As can be seen from figure 2.5 a) and from equation (2.33), the width of the interference area in regards to the delay τ is dependent on the bandwidth of the photons. This is intuitive since with the decreasing bandwidth, the coherence length of the photons increases, making the length in which the pair might interfere longer [42]. The reason that the normalized coincidence probability is 0.5 outside of the interference area is because of the classical probabilities of a beamsplitter interaction as seen in figure 2.5 b) [41]. These probabilities mean that in an ideal case 50% of the single photons randomly exit the BS together, when no two-photon interference is present. This probability is then increased to a 100% if they interfere perfectly.

Visibility is usually the value that is used to characterize how good interference is. For HOM

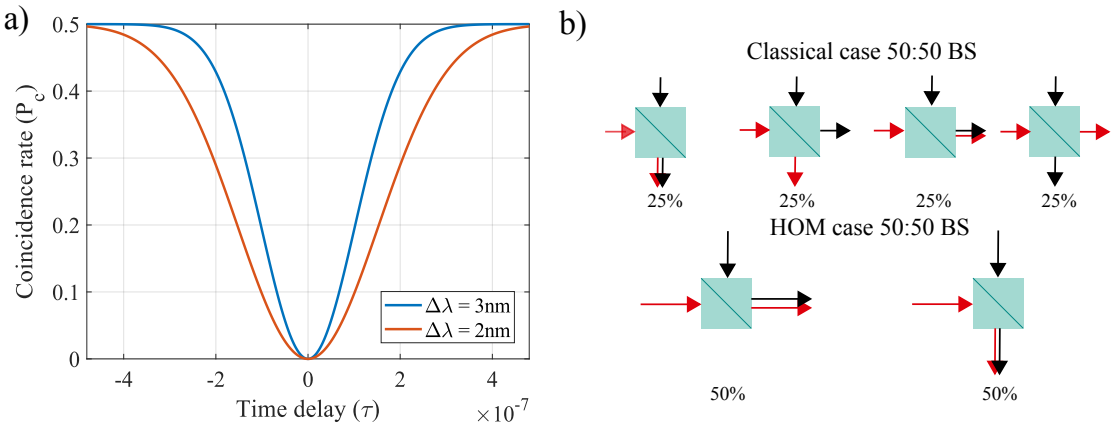

Figure 2.5. *In a) there is a curve representing the theoretical 2 photon coincidence detection rate as the BS arrival time delay of the photons is varied. The widths of the interference dips correspond to a 3nm and a 2nm wide gaussian wavelength distribution centered at 810nm, and the data is simulated using equation (2.33). In b) there is a simple representation of the operation of a 50:50 beamsplitter, in regular operation (classical) and in the HOM interference case. Now the arrows represent a single photon and the photons are indistinguishable in the HOM case.*

interference, it is usually defined by comparing the quantum mechanical detection probability to the corresponding classical one as in [41]

$$V = \frac{P_{CL} - P_{QM}}{P_{CL}}. \tag{2.34}$$

For the classical coincidence rate we have the equation $P_{CL} = |r_{ab}r_{ba}|^2 + |t_{aa}t_{bb}|^2$, where the indices a and b correspond to the previously defined paths and the coefficients r and t are the Fresnel reflection and transmission coefficients. This general form takes losses in the beamsplitter into account. For a symmetric case of $r_{ab} = r_{ba} = \sqrt{R}$ and $t_{aa} = t_{bb} = \sqrt{T}$, when the photons are perfectly indistinguishable our visibility can be simplified into the form

$$V = \frac{2RT}{R^2 + T^2}, \tag{2.35}$$

which is a visibility factor already derived by Hong, Ou and Mandel in [42].

This photon bunching in a regular beamsplitter is the most often used two photon interference phenomena and key in quantum information tasks, e.g. in photonic entangling gates [43]. It is also useful as an entangling gate for "NOON" states where, e.g. two photons, can be only found in one output path [44]. Additionally, it is used to characterize the distinguishability between two photons from one or multiple sources, since the visibility of the interference depends on how similar all of the photon properties are with each other [45]. HOM interference is also a great tool for exploring the fundamental nature of quantum interference effects [46].

2.4 Transverse-spatial modes of light

Now that we have an understanding of quantum states, and know how to generate single photons, we need to introduce the single photon degrees of freedom that we will be focusing on in this thesis. These degrees of freedom are the transverse field components of collimated light. In order to use them for quantum information tasks, we need to discretize these field components in some way. We do this with sets of orthogonal field structures that are stable forms of a collimated light beams transverse field. More specifically, we will be concentrating on the paraxial regime of light beams and investigating the structure of these beams in the plane transverse to the propagation direction of the beam. But most importantly for us though, as mentioned before, the transverse beam-structure can be sectioned into a discrete infinite-dimensional Hilbert space. This state space can be used in quantum communication and computation tasks, instead of the two-dimensional polarization state-space we focused on in section 2.1.1 [3]. In order to use these discrete states in any experimental task we first need to know what these orthogonal states are, so that we can discretize this degree of freedom with. In this section we will follow the derivation of these structures in Andrews' and Babiker's book [47].

To derive a description for EM-field shape in free-space, an obvious place to start are the free-space wave equations for lights electric field and magnetic field

$$\begin{aligned} \nabla^2\underline{\mathbf{E}} - \frac{1}{c^2}\frac{\partial^2}{\partial t^2}\underline{\mathbf{E}} = 0 \\ \nabla^2\underline{\mathbf{B}} - \frac{1}{c^2}\frac{\partial^2}{\partial t^2}\underline{\mathbf{B}} = 0, \end{aligned} \tag{2.36}$$

where $c = 1/\sqrt{\varepsilon_0\mu_0}$ is the speed of light in vacuum and μ_0 is the vacuum permeability [27]. These can be derived from Maxwell's equations when setting the charge distribution and charge current to zero, i.e. in vacuum or conditions approximating air. Any form of an EM-field that fulfills the above equation is a free-space light wave or EM-wave. We will now focus on the representation of the electric field and use the initial assumption that our EM-wave is a monochromatic wave, i.e. in the complex form $\underline{\mathbf{E}}(\underline{\mathbf{r}},t) = \underline{\mathbf{E}}'(\underline{\mathbf{r}})\exp(-i\omega t)$. With this assumption we get the Helmholtz equation

$$\nabla^2\underline{\mathbf{E}} - k^2\underline{\mathbf{E}} = 0, \tag{2.37}$$

where $k = \omega/c$ is the wave number and ω is the angular frequency. Further, we can restrict our light, or electro-magnetic field, to the paraxial regime where $\sqrt{k_x^2 + k_y^2} = \kappa << k_z$, if z is our beams propagation direction. This is because, in the paraxial regime, the wave vectors are mostly collinear with the optical axis of the beam (here the z-axis). This allows us to only use the first two orders of the taylor approximation for $k_z = \sqrt{k^2 - \kappa^2} \approx k - \frac{\kappa^2}{2k}$. Next, we will only focus on the electric field amplitude ε, which is just the electric field strength without the polarization $\underline{\mathbf{E}} = \underline{\mathbf{p}}\varepsilon$. With the paraxial approximation and another ansatz of the solution $\varepsilon(\underline{\mathbf{r}},t) = u(\underline{\mathbf{r}})\exp(i(kz - \omega t))$, where $u(\underline{\mathbf{r}})$ is the complex amplitude of the transverse electric-field, we can input the ansatz to the

Helmholtz equation and simplify it to get

$$\nabla_{x,y} u + 2ik\frac{\partial}{\partial z}u = 0. \tag{2.38}$$

Which is the so-called paraxial wave equation. [47]

Note that even though the light was assumed to be monochromatic, the paraxial wave equation allows for multiple different wavelengths due to the superposition principle. This principle simply states that for any two solutions to the wave equation, the sum of those two is also a solution to the wave equation [27]. This feature can simply be understood from the linearity of derivatives.

2.4.1 Laguerre-Gauss modes

If solving the paraxial wave equation (2.38) in cylindrical coordinates, we get an orthonormal set of solutions when we employ the associated Laguerre polynomials [48]

$$L_n^k(x) = \sum_{m=0}^{n} (-1)^m \frac{(n+k)!}{(n-m)!(k+m)!m!}x^m. \tag{2.39}$$

This set of orthonormal transverse field modes, called Laguerre-Gauss (LG) modes, are described by the complex amplitude

$$\begin{aligned} u_{l,p}^{LG}(\rho,\varphi,z) = \frac{C_{l,p}^{LG}}{\sqrt{w(z)}}\left(\frac{\rho\sqrt{2}}{w(z)}\right)^{|l|} \exp\left(-\frac{\rho^2}{w^2(z)}\right) L_p^{|l|}\left(\frac{2\rho^2}{w^2(z)}\right) \\ \exp\left(-ik\frac{\rho^2 z}{2(z_R^2+z^2)} + il\varphi - i(2p+|l|+1)\chi_G(z)\right), \end{aligned} \tag{2.40}$$

where ρ is the radius from the beam center, φ is the azimuthal angle, $C_{l,p}^{LG} = \sqrt{2^{|l|+1}p!/[\pi(p+|l|)]}$ is a normalization constant, $w(z)^2 = w_0^2\left[1+(z/z_R)^2\right]$ is the Gaussian beam radius, $z_R = \pi w_0^2/\lambda$ is the Rayleigh range, λ is the wavelength of the light used, w_0 is the beam waist or beam radius at $z=0$, and $(2p+|l|+1)\chi_G$ is the Gouy phase where $\chi_G = \tan^{-1} z/z_R$. The Rayleigh range is used to define the near field of a Gaussian beam and the Gouy phase describes the evolution of the wavefront during propagation. The Gaussian beam radius is defined as the distance from the beam center to the radius where the local field intensity is $1/e^2$ times the maximum. The index p gives the amount of π phase jumps in the radial structure of the beam. Since a phase jump results in an undefined phase at that position, this results in p intensity minima in the radial structure as can be seen in figure 2.6. Because of this, modes with $l=0$ and $p\neq 0$ are usually called radial modes. The index l corresponds to the number of 2π phase ramps in the azimuthal beam structure as can also be seen in figure 2.6. This results in some interesting angular properties that become apparent when looking at the wavefront picture. Since the wavefront is a plane of uniform phase, the phase structure results in l intertwined helical planes in the wavefront that have a slightly tilted wave vectors perpendicular to them [3]. Two examples of these helical wavefronts can be seen in figure 2.7. [47, ch.1]

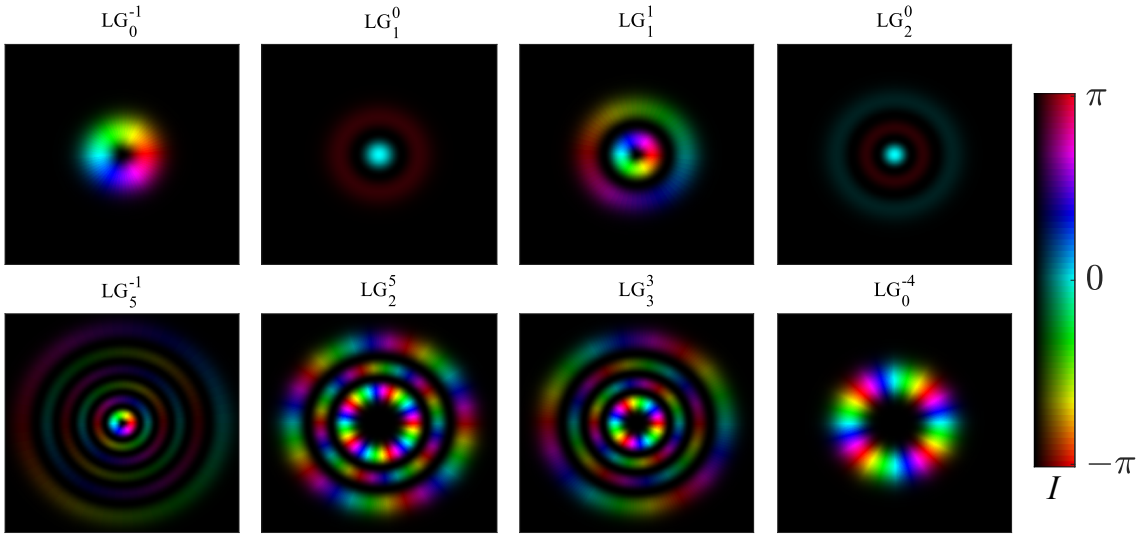

Figure 2.6. *Examples of different Laguerre-Gauss modes in the transverse two-dimensional Cartesian plane. The upper and lower indices refer to the l and p indices respectively. The color-mapping represents the phase of the field at different points of the transverse plain and the brightness of the colors signify the intensity of the field at that coordinate.*

One of the important features of any mode family is the orthogonality, which means that there isn't any overlap between different modes of the family, i.e.

$$\left\langle u^{LG}_{l_1,p_1} \middle| u^{LG}_{l_2,p_2} \right\rangle = \int_0^{2\pi} \int_0^{\infty} u^{LG*}_{l1,p1}(r,\phi) u^{LG}_{l2,p2}(r,\phi) r dr d\phi = \delta_{l_1,l_2} \delta_{p_1,p_2}, \tag{2.41}$$

if we assume that the wavelengths and beam radii match. Additionally, due to the completeness of the mode family, any arbitrary transverse structure of a collimated beam can be described in the basis of LG-modes. Due to the high-dimensionality of this orthonormal state basis, i.e. due to the multiple possible combinations of l and p, if we can generate and measure light beams with these transverse structures, we can transmit much more than two bit-values of information using this degree of freedom. Importantly for quantum communication applications, this degree of freedom can also be used with single photon states. What this entails is that if we assign bit-values of up to N on a set of these eigenmodes, we can effectively encode $log_2 N$ binary bits on a light beam or a single photon using the orthogonal spatial modes of different indices l and p [3]. By only using the l-index of these mode structures, data rates of up to one Tbit/s have been achieved in laboratory conditions [3]. Inclusion of the p-index could increase this rate, due to the increased state space size, but thus far there have been problems caused by the complexity and inefficiencies of methods required in preparing and measuring the complete transverse beam structures [49, 50]. Besides the generation and detection, the biggest challenge in implementing any transverse-spatial structure into communication schemes is the stability of the modes during long distance transmissions. In air and other isotropic channels, over long distances, turbulence can cause problems because of the distortion it might cause to the transverse structure, and in multi-mode fibers, mode mixing causes the intended information to be scrambled [3, 10, 51].

Another interesting feature of the LG-mode family is the fact that the mode index l is connected to

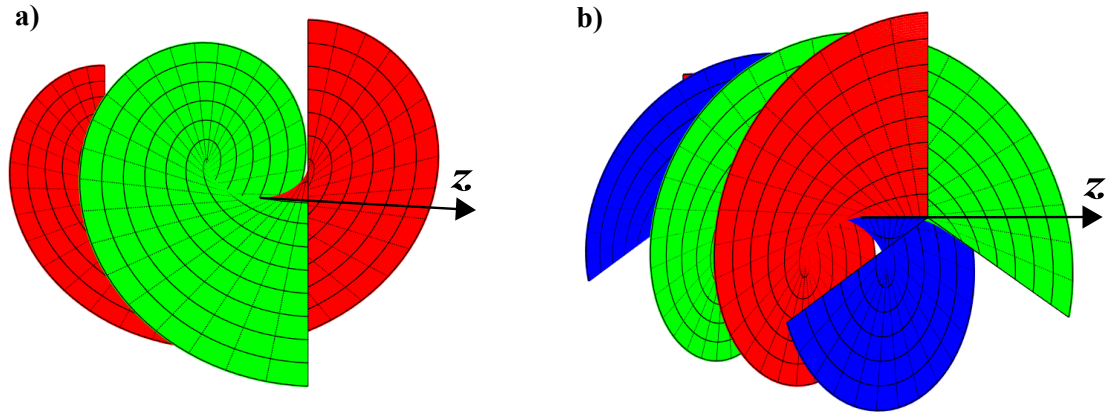

Figure 2.7. *Wavefronts for a) an LG_0^{-2} and b) an LG_0^3 beam. Here it is visible that the magnitude of l tells how many intertwined helical planes with constant phase exist for a beam mode. The sign of l specifies the direction of rotation for the helices. Since the wave vector k is defined to be perpendicular to a wavefront, the tilted wave vectors connected to these helices give an intuition on the angular momentum connected to the structures [27, ch.2]. The colors are used to separate the different intertwined helices.*

an orbital angular momentum (OAM) for photons with these types of transverse field-structures. Hence, LG-mode structures with $l \neq 0$ and $p = 0$ are commonly called OAM-modes. This is the second type of angular momentum light can have. Its more familiar counterpart, spin angular momentum (SAM) is connected to the circular polarization of light. Its connection to spin is caused by the fact that when absorbed by a small particle it causes the particle to spin around its own symmetry axis. The l-index dependent angular momentum is called orbital since, in contrast to the SAM, when a light beam in an OAM-mode interacts with a small particle, the particle would start orbiting around the light beams optical-axis. This can be visualized from the tilted k-vectors connected to the tilted wavefront in figure 2.7. Also, due to the unbound nature of the azimuthal index l, the strength of OAM carried by a photon can be very large, i.e. $l\hbar$. Whereas SAM per photon can only be $\pm\hbar$. However, this separation of SAM and OAM can only be done in the paraxial regime and the two angular momenta start to couple if we, for example, tightly focus our beam. [52]

As a side note, the OAM of light has already been harnessed for manipulating matter. In optical traps SAM has been used to spin certain types of particles around their own symmetry axis, and as expected, OAM has been used for orbiting particles around an axis [52]. This makes quite complex light traps possible, by using the OAM of light. Additionally, the discrete OAM-modes have been used in some quantum optics applications, e.g. in entanglement experiments [53] and quantum communication [8, 54].

2.4.2 Hermite-Gauss modes

The aforementioned LG-mode family isn't the only orthogonal mode family capable of fully describing the transverse field-structures of paraxial beams. The second mode family we will utilize is derived by solving the paraxial wave equation (2.38) in the Cartesian coordinates. The mode family is called Hermite-Gaussian (HG) modes. These modes can be separated into x and y dependent parts of the complex amplitude, i.e. $u^{HG}_{n,m}(x,y,z) = u^{HG}_{n}(x,z)u^{HG}_{m}(y,z)$, such that

$$u^{HG}_{n}(x,z) = \frac{C^{HG}_{n}}{\sqrt{w(z)}} \exp\left(ik\frac{x^2 z}{2(z_R^2+z^2)} - \frac{x^2}{w^2(z)} - i\left(n+\frac{1}{2}\right)\chi_G(z)\right) H_n\left(\frac{\sqrt{2}x}{w(z)}\right), \tag{2.42}$$

where H_n is the Hermite polynomial, $C^{HG}_{n} = \sqrt{1/(2^n n!)}(2/\pi)^{1/4}$ is a normalization constant, and and $(n+\frac{1}{2})\chi_G$ is the Gouy phase [47, ch.1]. The same equation works similarly for $u^{HG}_{m}(y,z)$. Here the indices n and m describe the amount of π phase jumps in the x and y directions, similarly to the way the p-index describes the phase jumps in the radial structure of LG-modes. Another analogous property between HG- and LG-modes is the orthogonality between HG-modes with differing indices n and m, hence the inner product $\left\langle u^{HG}_{n_1,m_1} \middle| u^{HG}_{n_2,m_2} \right\rangle = \delta_{n_1,n_2}\delta_{m_1,m_2}$. But as before, this relation holds only if the effective beam radii match for each mode. As can be seen in figure 2.8, due to the HG-modes being derived in the Cartesian coordinates, these modes have symmetric intensity structures in regards to the x and y axes.

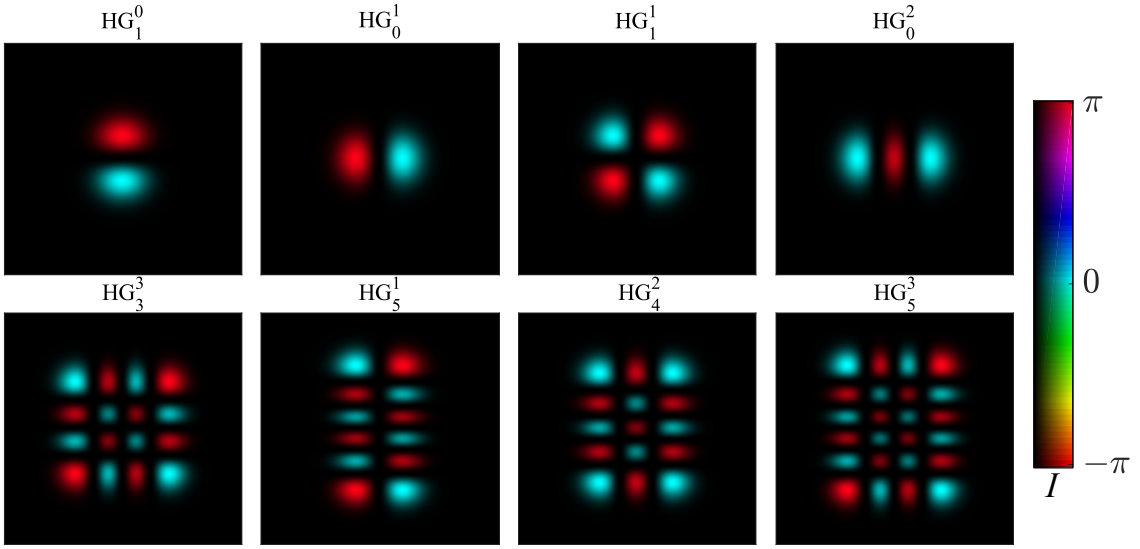

Figure 2.8. *Examples of different Hermite-Gauss modes. The upper and lower indices refer to the n and m indices respectively. The color-mapping represents the phase of the field at different points of the transverse plain and the lighter the area is the more intense the field is at that coordinate.*

Since these modes also compose a complete orthogonal set in the transverse spatial degree of freedom, they have most of the same possible benefits LG-modes have in applications. Furthermore, they have been easier to generate in the early days of spatial mode research, since the phase jumps and intensity minima can be introduced by simple amplitude masks, e.g. with a wire in a laser cavity [55]. However, one clear disadvantage is the cartesian symmetry, since most of our com-

munication channels, e.g. optical fibers, have a circular symmetry [3]. The circular symmetry of LG-modes is also beneficial with free-space systems [3].

2.4.3 Hong-Ou-Mandel interference between Transverse-spatial modes

Previously, we introduced HOM interference that occurs between different photon paths in a beamsplitter. However, path is only a single degree of freedom for a photon. Thus, if we can make a device that creates superpositions between spatial modes, that are similar to the ones a beamsplitter creates between paths, the same effect should be observed in this degree of freedom. Moreover, if we can build a device capable of doing this between any pair of spatial modes, we would have a two-photon interference between any set of spatial modes. This device would then open new possibilities in applications of spatial modes.

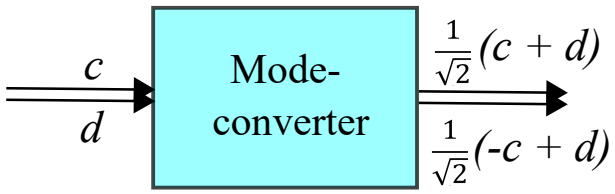

Figure 2.9. *A simple visualization of a mode-converter capable of converting two input photons in orthogonal spatial modes into superposition spatial modes between the original input modes. This operation is analogous to the way a beamsplitter outputs photons in superpositions of two different photon paths. Except for this mode-converter the superposition would be between different spatial modes.*

To accomplish this "spatial mode beamsplitter" we would need a device similar to the one displayed in figure 2.9. In this figure the two inputs c and d would be in the same path but different orthogonal spatial modes. If we then have a unitary spatial-mode converter that transforms both of these input modes into a superposition of two orthogonal spatial modes, we should see bunching when inputting two indistinguishable photons simultaneously into this device. A simple two-dimensional example of this type of a unitary mode-conversion is

$$\hat{U}_{MC} = \frac{1}{\sqrt{2}} \begin{bmatrix} 1 & 1 \\ -1 & 1 \end{bmatrix}, \tag{2.43}$$

where MC stands for mode-converter. We now choose the input states of our example to be the LG-modes $c = LG_0^1 = |+1\rangle$ and $d = LG_0^{-1} = |-1\rangle$, for the photons c and d respectively. Then this described mode-converter would transform the states into the superposition states $\frac{1}{\sqrt{2}}(|+1\rangle + |-1\rangle)$ and $\frac{1}{\sqrt{2}}(-|+1\rangle + |-1\rangle)$, that are mutually orthogonal in a separate MUB. For the case of two photons, indistinguishable in all other degrees of freedom, we get a familiar looking output

state from the mode-converter that is of the form

$$\begin{aligned}|\Psi_{out,MC}\rangle =& \hat{U}_{BS}\,\hat{a}^{\dagger}_{+1}\hat{a}^{\dagger}_{-1}\,|vac\rangle = \frac{1}{2}\left((\hat{a}^{\dagger}_{+1}+\hat{a}^{\dagger}_{-1})(-\hat{a}^{\dagger}_{+1}+\hat{a}^{\dagger}_{-1})\right)|vac\rangle \\ =& \frac{1}{2}\left(-\hat{a}^{\dagger 2}_{+1}+\hat{a}^{\dagger}_{+1}\hat{a}^{\dagger}_{-1}-\hat{a}^{\dagger}_{+1}\hat{a}^{\dagger}_{-1}+\hat{a}^{\dagger 2}_{-1}\right)|vac\rangle \\ =& \frac{1}{2}\left(-\hat{a}^{\dagger 2}_{+1}+\hat{a}^{\dagger 2}_{-1}\right)|vac\rangle \\ =& \frac{1}{\sqrt{2}}\left(-|2_{+1},0_{-1}\rangle+|0_{+1},2_{-1}\rangle\right).\end{aligned} \tag{2.44}$$

This output state means that after the mode-conversion, the two indistinguishable photons should interfere and end up in the same spatial mode. The interference still happens in the spatial domain, but the photons stay in the same beam path during the whole process. Additionally, if we have a simple way of producing these unitary spatial mode conversions, this process should be easy to scale into e.g. interference between three spatial modes. This three-dimensional operation would then be analogous to two photon interference in a three-way beamsplitter, i.e. tritter.

3 MANIPULATING THE TRANSVERSE SPATIAL DEGREE OF FREEDOM

In this thesis, the most important experimental tasks were to imprint transverse-spatial mode-structures on light beams, to convert between these modes, and to measure the transverse-spatial structure of our laser beams and single photons. This means that we require a device that we can use to perform all these tasks. Our device of choice, for these applications, is the phase-only liquid crystal spatial light modulator (SLM) which we will briefly introduce in this chapter. We will also introduce some common spatial mode generation and measurement methods we will be implementing with these SLMs. Most importantly however, in this chapter we will introduce the method we used to construct unitary transformations between spatial modes, called wavefront matching (WFM).

3.1 Wavefront matching

Wavefront matching is a method utilizing multi-plane light conversion (MPLC). In very basic terms, MPLC's consist of a certain number of phase-modulation planes with free-space propagations between them. Then, with these phase-modulations the system can transform the transverse structure of a beam. A simple sketch of this type of a conversion is shown in figure 3.1, for a simultaneous transformation of two spatial modes. The WFM algorithm is the tool that generates these phase-modulations in a way that the wanted spatial-mode conversions are performed in the MPLC. For the WFM algorithm, we need a predefined set of input spatial modes and the corresponding output modes. Then we need to set the number of phase-modulation planes we want to use in the conversion, along with the propagation distance between the modulation planes. The goal of the algorithm is to simulate this specific MPLC configuration and optimize the phase-modulations in a way that allows the wanted conversion to happen in the simulated system. In principle, this method can then generate phase-modulations to perform any arbitrary unitary mode transformation, as long as the conversion is physical, and we employ enough phase-modulating planes.

This method has been previously used in waveguide applications [56], but the free-space version we employ here was introduced by Fontaine et al. for a different type of task, i.e. spatial mode de-multiplexing [16]. The way the optimization algorithm works is by first propagating the input modes forwards through all of our phase screens that are initially blank screens with zero phase modulation at all coordinates. Secondly the desired output modes are backpropagated through the

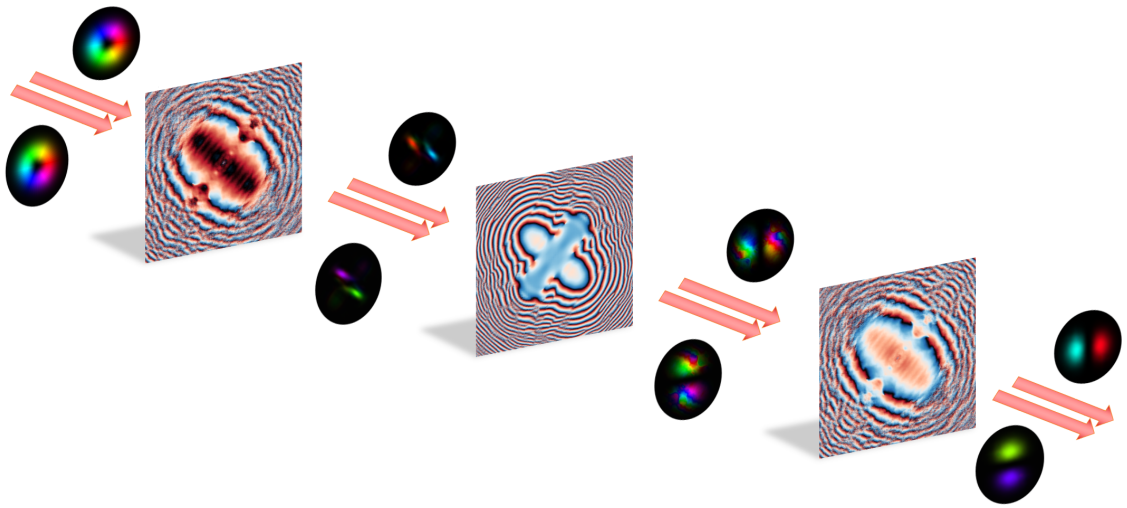

Figure 3.1. *Wavefront matching concept. The example here employs three phase screens and two input modes. The colors on the phase screens signify the different phase changes different parts of the phase screen imprint on an incoming light beam. Each mode transforms in a different way if propagated through the centers of the same phase screens with appropriate propagation distances in between. The optimization process updates phase screens computationally by comparing the shown intermediate modes. The comparison is done between forward propagated input modes and backwards propagated output modes. The conversion shown here transforms an LG_0^1 mode into a coherent superposition of LG_0^1 and LG_0^{-1}. Additionally, it transforms LG_0^{-1} into an orthogonal superposition (i.e. it acts as a Hadamard-gate). The spatial-mode color-mapping displays the phase and intensity and is explained in figure 5.1.*

same phase screens. The simulated propagation of these modes was done using split step propagation, also known as angular spectrum propagation, which is a Fourier optics method [57, ch.3]. After propagating all of the modes forwards and backwards, the algorithm begins to change the phase screens starting from the first or the last phase-modulation plane. On this plane the forward-propagated input and backward-propagated output modes are compared. The comparison between the input and output modes is done by calculating the overlap between the transverse complex amplitudes of the forward propagated input modes and the back-propagated output modes. This overlap between modes indexed i and j at the phase screen t is calculated using

$$o_{tij}(x,y) = F_i(x,y,t)\overline{B_j(x,y,t)}e^{i\Phi_t(x,y)}, \tag{3.1}$$

where Φ_t is the phase structure of phase screen t (initially zeros), $F_i(x,y,t)$ is the complex amplitude of the forwards propagated beam mode at phase screen t, and $B_j(x,y,t)$ is the same for the backwards propagated beam mode. The phase screen is updated using a formula derived using the gradient descent optimization algorithm [16]

$$\Delta\Phi_t(x,y) = -\arg\Big(\sum_i o_{tii}(x,y)e^{-i\phi_i}\Big), \tag{3.2}$$

where $\phi_i = \langle \arg(o_{tii}(x,y)) \rangle$ is just the average phase overlap between the corresponding input and output modes. The indices i signify that the ith input mode and the corresponding ith output mode are the ones being compared, i.e. we only compare the input modes with the output mode we want

to convert it into. The summation over different indices i means that, when designing a conversion for multiple modes, we sum the phase differences of all our different output-input mode pairs onto the phase-modulation on plane t. In effect, the term $\Delta\Phi_t(x,y)$ introduces a phase change onto the phase-modulation plane t that reduce the differences between the forwards propagated input spatial modes and the back-propagated output spatial modes at this plane. After the phase-modulation has been updated, we can imprint it on our forward and backward propagating beams by simulating their propagation through the system as necessary. Then the algorithm can move onto comparing overlaps at the next phase-modulation plane. After updating all of the phase-modulations, the whole process can then be repeated multiple times for all of the phase screens. This repetition is done by restarting the whole procedure, with the updated phase-modulations from the previous iteration as a starting point. Finally, unless the conversion isn't physical or we don't have enough phase-modulation planes, the overlap between the simulated MPLC output mode and the desired output mode should converge towards unity after multiple iterations.

With this method it would be possible to convert almost any arbitrary spatial mode into any other spatial mode, if the number of phase screens is large enough to account for the number and complexity of the modes used. Of course, when using SLMs for these phase transformations as we did, if we scale the number of phase screens, the efficiency is reduced since one reflection off of an SLM doesn't modulate all of the input light (e.g. $\sim$75% for the Holoeye SLMs we used). But this problem could possibly be overcome, or at least reduced, e.g. by fabricating more efficient static optical phase elements as in [58].

3.2 Spatial light modulators

The device we will be using to imprint these aforementioned phase-modulations is a spatial light modulator. These devices, as the name suggests, modulate the transverse field-structure of the light incident on the device. Effectively this is achieved either by modulating the intensity, phase, or both properties of the light field in a different way at different locations (pixels) of the device [59]. These methods are also used more commonly in projectors.

The type of SLMs we use in our work is phase-only liquid crystal SLMs. These work like electrically adjustable phase-screens that imprint a transverse phase structure onto the incoming beam, effectively changing the wavefront of the beam. The liquid crystals of the device introduce a phase delay to the light wave propagating through it. This is caused by the birefringence exhibited by the liquid crystals, and hence we can change the effective phase delay by changing the orientation of the crystal in relation to the incoming lights polarization. The liquid crystals are small and rice grain shaped; therefore they can be laid out in a grid to achieve a two-dimensional matrix of local phase delays. Since the effective birefringence of the crystals is related to the orientation of the crystals, we need to be able to rotate the crystals individually to display any pixelized two-dimensional phase-structure on the SLM. This orientation can be adjusted with an electric current for nematic liquid crystals, and by using these types of liquid crystals, we have a device that introduces a different phase delay at different pixels by changing the crystal orientations with electric currents. [60]

The orientation of the crystals must be specific in relation to the input light polarization, in order for the device to work consistently. Therefore, the crystal long axes have to be parallel to the lights polarization direction, in order to achieve a phase-only modulation [60, 61]. This usually means that the SLMs only work with a single linear polarization.

These same liquid crystals are also used in liquid crystal displays. But in these displays, amplitude modulation is more commonly used, which usually involves polarizers. In these amplitude masking configurations the liquid crystals adjust the lights polarization direction and consequently the absorption of light at the polarizers [59].

The SLMs we used were Holoeye Pluto-2 SLMs with a roughly 75% modulation efficiency for light with a wavelength of 810nm. Because of this inefficiency, we need to add a diffraction grating to all our phase screens, so that we have the wanted phase structures in the first diffraction order of these hologram structures. We add the grating so that we won't have a mix of modulated and unmodulated light in the same beam path.

The SLMs we used also required some calibrations before we were able to use them properly. This calibration involved linking the grayscale values displayed on the SLMs to actual phase shifts the device induces. This calibration was done using an interference setup described in [34].

3.3 Spatial mode generation and detection

Besides implementing the WFM, the second most important tasks we need to perform with these SLMs are to generate beams with different spatial modes and to measure any light beams transverse-spatial structure. Both tasks are complex since we only have our phase altering SLMs to work with and the spatial modes also have varying intensity structures that require some amplitude structure modulations in generation and measurements. The complexity of the spatial mode structures can be seen in the figures presented in section 2.4.

The first task of generating different spatial modes gets additional complexity since we have to start off with a Gaussian beam instead of an ideal plane wave. The method we employ to generate spatial modes in our experiments combines the phase altering properties of our phase only SLMs with an effective amplitude mask. This method is described in more detail in [49]. In short, this method uses a diffraction grating and imprints the wanted phase on the first diffraction order of light interacting with the grating. If the diffraction grating is then selectively applied only on certain areas, we can effectively manipulate the intensity structure of the first diffraction order with a phase-only SLM. In practice, this manipulation of the spatial intensity structure is done by multiplying the phase only hologram structure with an intensity dependant masking function. The phase only hologram structure already includes an efficient blazed diffraction grating before the amplitude masking. The masking function is of the form

$$M(x,y) = 1 + \frac{1}{\pi}\,\mathrm{sinc}^{-1}(A(x,y)), \tag{3.3}$$

where $A(x,y)$ is the wanted transverse-spatial amplitude structure of the beam. Since the function

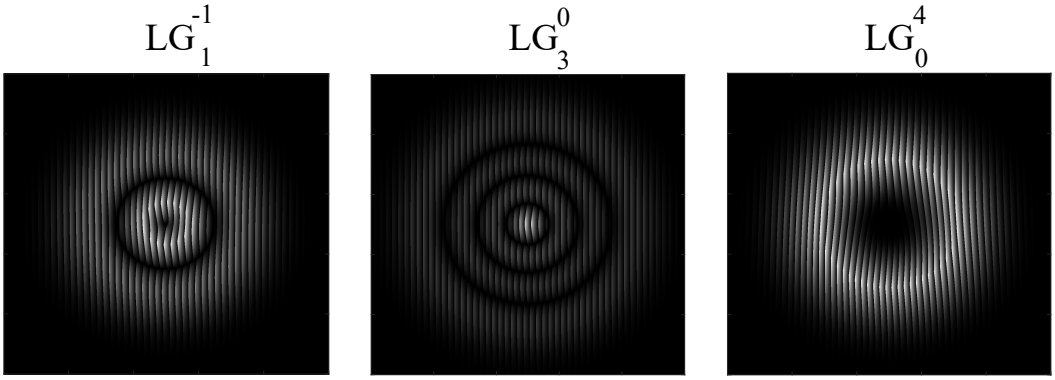

Figure 3.2. *Examples of different amplitude masked LG-mode generation holograms calculated using equation (3.5). Each of the holograms is overlaid with a blazed grating. These holograms are also used in the intensity flattening protocol described later in this section.*

M is only masking the intensity, it is bounded in the interval $M \in [0,1]$. Due to the additional phase distortions this causes in the mode structure of the first diffraction order, an additional phase term $\pi M(x,y)$ is added to the total phase modulation. Then the phase we want to imprint is of the form

$$F = \Phi(x,y) - \pi M(x,y), \tag{3.4}$$

where $\Phi(x,y)$ is the phase structure of the desired spatial mode. We can then derive the final hologram structure by including the grating term and the amplitude masking. The final hologram is then

$$T(m,n) = \exp\left(iM(m,n)\text{Mod}\left(F(m,n) + \frac{2\pi}{\Lambda_x} + \frac{2\pi}{\Lambda_y}, 2\pi\right)\right), \tag{3.5}$$

where Λ_x and Λ_y describe the grating period for both the x and y directions. In the above equation we have changed our cartesian coordinates (x,y) to pixel coordinates (m,n) because of the discrete SLM pixels. A few examples of these types of holograms, for generating some LG-modes, are shown in figure 3.2.

Even though this generation method produces the spatial modes fairly accurately, it still isn't perfect. The input field is assumed to be a plane wave in its derivation [49], and even though this is a good approximation for the large Gaussian input beams we use, the intensity profile might not be optimally flat. Also, due to the amplitude masking, the method is very lossy. Of course, the losses scale with the amount of amplitude masking but the mode fidelity is also increased with increased amplitude masking. This is due to the fact that if we only select the central region of our input Gaussian for amplitude masking, we will have a relatively flat amplitude profile in this small region of the Gaussian. Of course, this is limited by the size of our SLM pixels.

The second task is measuring the transverse-spatial mode structure of our beams and for this task we employ two different methods. The simpler method only works for the azimuthal structure of the LG-modes and has been the most common method for measuring the orbital angular momentum of photons [62]. The holograms this method requires consist simply of an azimuthal phase ramp with an added grating. Of course, this whole structure is again wrapped back in to a single

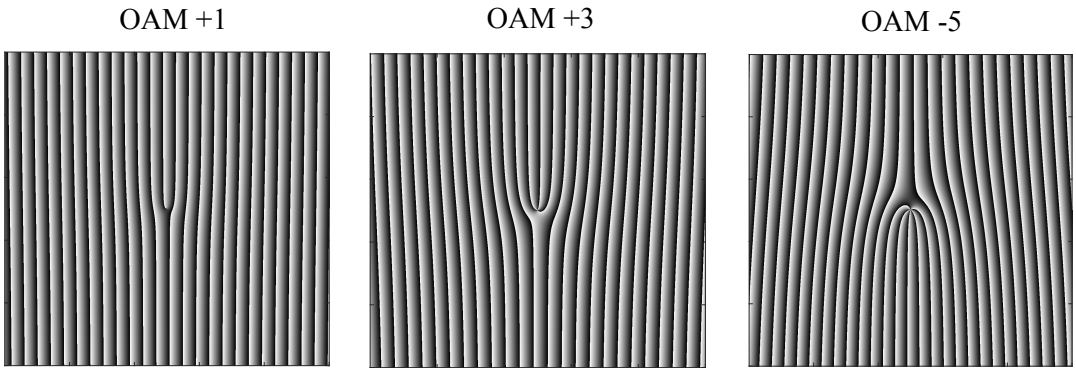

Figure 3.3. *So-called phase flattening holograms. The added gratings are the same on all of the images and the differences are in the amount of OAM the holograms imprint on the first diffraction order of a beam that interacts with them. The sign of the imprinted OAM value changes if we move the hologram dislocations from the upper half to the lower half or vice versa.*

2π interval with a modulus operation. These holograms then remove or add a certain amount of OAM from light interacting with it [63]. This means that if, for example, the holograms phase changes 6π on a single azimuthal rotation, the hologram adds three quanta of OAM to the impinging light field. Unless the impinging field already has a “negative", i.e. opposite direction, OAM. In this case the hologram would remove three quanta of “negative" OAM from the beam. As an example, if our impinging field has an OAM of $-2\hbar$ and our hologram adds three positive OAM quanta on it, the output field has an OAM value of $+1\hbar$. Again, the wanted phase-change happens only in the first diffraction order of these holograms. The first diffraction order can then be filtered by coupling the first diffraction order into a single mode fiber (SMF). This SMF filtering lets only Gaussian modes, i.e. modes with no OAM or other spatial structures, to couple into the SMF efficiently. Therefore, when cascading the SMF coupling with our hologram, we only couple in light that previously had the OAM-value the hologram removes [64].

A few examples of these kinds of holograms can be found in figure 3.3. In this figure the OAM value tells us how many quanta of OAM the hologram imprints on a beam. The result from summing up a blazed grating and an azimuthal phase ramp is a blazed grating with dislocations in the center, as can be seen from the figure 3.3. The number of dislocations corresponds to the quanta of OAM the hologram adds or removes, and the direction of the dislocation tells if it will add a “positive" or a “negative" OAM value. To reiterate, these negative and positive OAM values refer to the signs of the LG-mode index l which is connected to the direction of the OAM of the beam.

The second measurement method we use can measure the full transverse structure of a beam. It also relies on a SMF to only filter in Gaussian beam profiles efficiently. The method is called intensity-flattening by its authors in [50]. This method is almost the same process as the previously introduced mode generation by amplitude masking but done in a reverse order. Hence, the method uses the same amplitude masked holograms displayed in figure 3.2, that flatten any helical phases and preferentially diffract certain transverse intensity structures that correspond to the structure we want to measure. The only problem then is that the SMF only couples in efficiently Gaussian

modes that are of a specific beam waist. This is circumvented by coupling in a larger beam than what we actually have. This allows the coupling of beams with larger, more complicated, intensity structures. Meaning that we could couple in structures that we couldn't normally couple efficiently if we used a smaller coupling waist with the SMF. Effectively, this can be seen as flattening the intensity structure of our beam into the central part of the bigger Gaussian that couples into the SMF. Now the sensitive part is adjusting this coupling waist. This is because, for bigger coupling waist to beam waist ratios, the visibility between measured modes increases, whereas the efficiency simultaneously decreases. Thus one can get an very accurate measurements of the spatial modes at the cost of longer measuring times caused by the losses [50].

4 QUANTUM INFORMATION TASKS

In this chapter we introduce two quantum information tasks that we performed in the experimental section of this thesis. We performed these two tasks with our unitary mode-conversion, since they require precise quantum state measurements. Hence, how well our converter performs in these tasks gauges the potential of the mode-conversion method.

4.1 Quantum Key Distribution

The first of these two tasks was quantum key distribution (QKD). In general terms, QKD is a method for generating and distributing a random encryption key that two communicating parties can use to encrypt and decrypt their messages. There are two major categories of QKD, entanglement-based protocols, and prepare and measure protocols. In the entanglement-based protocols, entangled pairs of particles are shared between the parties, and the key is established by measuring these entangled pairs [65]. The details are protocol dependent but the common element between all of these entanglement-based protocols is the security brought by entanglement. The principle behind this security is that, when an eavesdropper disturbs the entangled pair, the perfect correlations of entanglement are lost and that will be noticed by the communicating parties. The simpler to implement category is the prepare and measure protocols since those don't require entangled pairs. Because we will implement a test of a prepare and measure protocol, we will focus on those types of protocols here.

These prepare and measure protocols requires the sender (Alice) to be able to prepare the quantum states in at least two different MUBs of the chosen state space. Similarly, the receiver (Bob) needs to be able to measure the states in the same MUBs. In the protocol we will test in this thesis (BB84) [66], two MUBs are chosen, and in order to send and receive data securely with this protocol, Alice has to encode her bits randomly in one of the two MUBs. This means that each state in each MUB is assigned a bit value, e.g. 2 bit-values for a two-dimensional state space, and if Alice wants to send the value 0, she prepares it randomly in either of the MUBs and sends it. A simple sketch describing the protocol, along with an example of two-dimensional sets of states can be found in figure 4.1 Because of this random preparation, Bob and any eavesdroppers don't know which MUB to measure in and have to randomly choose a MUB. This random preparation in different MUBs is the key to the security of this scheme since measuring a single quantum state simultaneously in two different MUBs is impossible. Hence, if an eavesdropper is intercepting and measuring the sent quantum state, they would measure it inaccurately at least 50% of the time. Additionally, when measuring the state in the wrong MUB, the eavesdropper alters the state.

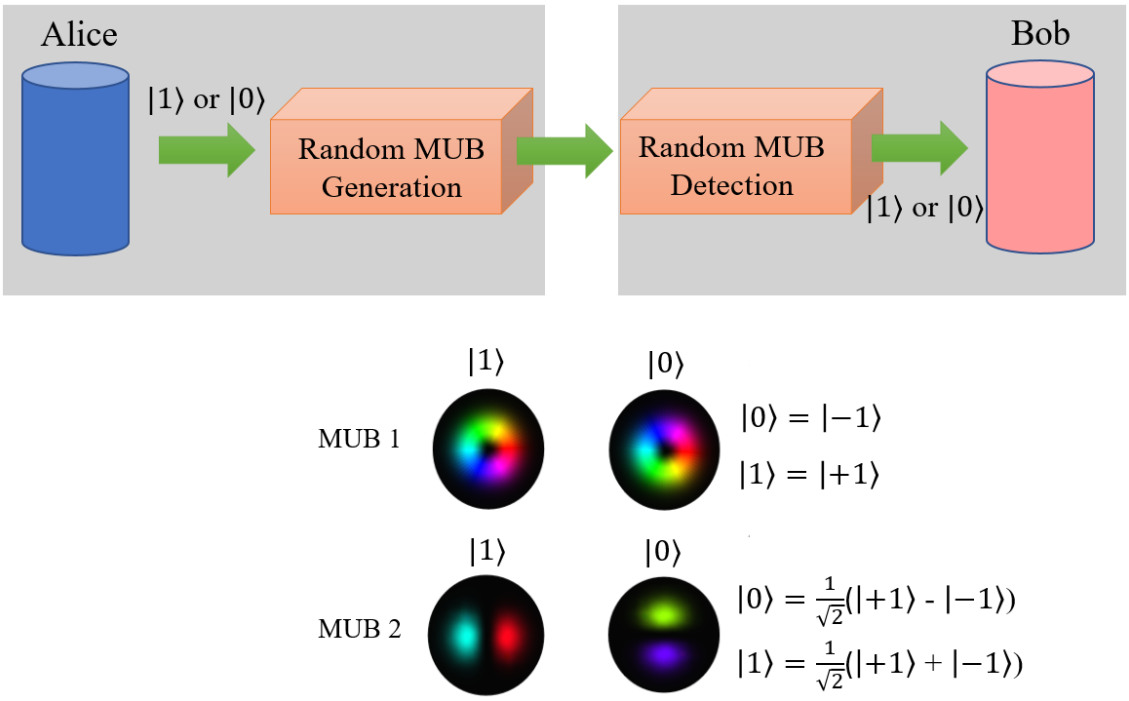

Figure 4.1. *A simple figure visualizing the process of QKD. In the upper half there is a simple representation of the prepare and measure process between Alice (sender) and Bob (receiver). In the lower half is one example of the possible bit-values that could be used in a two-dimensional BB84 protocol. The example is a two-dimensional set of LG-modes and their superpositions in a different MUB. The chosen LG-modes are* $LG_0^1 = |+1\rangle$ *and* $LG_0^{-1} = |-1\rangle$.

And, in order to not be detected, the eavesdropper would then have to transmit this altered state to Bob. This would then cause unexpected errors in Bobs results.

Regardless of any eavesdroppers, this randomness on its own results in unreliable data for half of the measurements Bob does. But if Bob and Alice, e.g. through a separate public channel, announce the MUBs they sent and measured each state in, they can post-select on measurements that were done in the correct MUB. This process of post-selection is usually called sifting. The correct measurements, that are left after this sifting, can then be used to generate the encryption key that only Alice and Bob knows. But before this is done, Bob and Alice need to check for eavesdropper induced errors before deciding on the key. Hence, they need to sacrifice a few of the successful measurements by comparing the measured states with the sent states over the public channel. After these comparisons, if the error rate doesn't indicate an eavesdropper, the remaining successful measurements are used to generate the secure encryption key. [19, 66]

4.1.1 Transverse-spatial modes in QKD

In addition to the previous two-dimensional example, these QKD-protocols can be implemented with higher-dimensional Hilbert spaces. An excellent candidate is the infinite-dimensional space of orthogonal spatial modes, since generating the different MUB states is quite easy for these modes. Hence, with any d-dimensional subset of spatial modes we have a theoretically possible

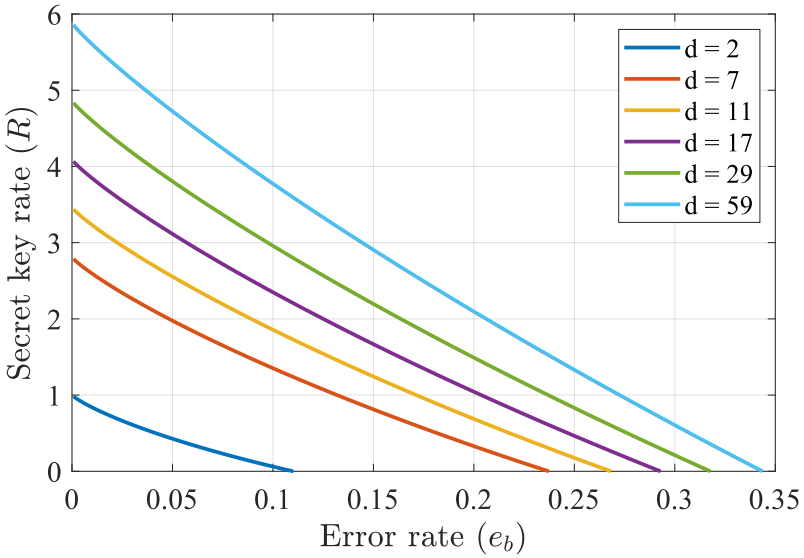

Figure 4.2. *A plot visualizing the relation between effective bit rate per measured photon as a function of bit error rate. In the legend, d signifies the state space dimensionality. The curves were calculated with equation (4.1). We can see from the plot that with higher-dimensional state spaces, the amount effective number of bits per measured photon is increased along with the robustness to errors.*

bit rate of $\log_2 d$ bits per measured photon [65] and the MUB states are achieved by just summing the set transverse field terms in specific ways to achieve new orthogonal sets of modes [21, 65]. For the common two-MUB QKD, our state space can be of any dimension bigger than one. However, if we want to include more than three MUBs, we need a power of prime dimensional state space, since we can only calculate the $d+1$ MUBs for state spaces of these dimensions [21]. Using more MUBs then results in more sifting but better robustness to errors [65, 67].

All this noise and impreciseness is usually quantified into a single variable called the bit error rate e_b, which is the average error we will have when measuring our state. This error rate can be used to define an effective secret key rate for high-dimensional QKD with two MUBs [67]

$$R = \log_2(d) - 2h^{(d)}(e_b), \tag{4.1}$$

where d is again the dimensionality of our state space and $h^{(d)}(x) = -x\log_2(x/(d-1)) - (1-x)\log_2(1-x)$. This secret key rate tells us how many bits each sifted photon adds to the generated encryption key. The previously mentioned increased robustness is observed as an increase in the maximum error allowed by the protocol with higher dimensions. This maximum error is defined as the error rate that causes our secret key rate to drop to zero. [65]. This increased key rate and robustness can be seen from figure 4.2.

One technical limitation related to these high-dimensional state bases is the ability to demultiplex the discretized spatial modes. Meaning that, if we are not able to measure any possible state of a single MUB at once, e.g. by sorting, we have to resort to filtering for a single state at a time. This measurement of all states in a MUB corresponds to a measurement that gives us the exact state of our system, if we choose the MUB correctly. When the protocol is performed

with single mode filtering measurements, the amount of losses increases. This happens since, if we filter in the correct MUB but with the wrong state, the only information gained is that the sent information is one of the other d-1 bit-values [65]. This, of course, lowers the maximum achievable key transmission rate in comparison to detection schemes able to distinguish between multiple possible photon states at once.

4.2 Quantum state tomography

The second quantum information task performed in the experimental section of this thesis is quantum state tomography. The general goal of this task is to reconstruct the density matrix of a quantum system by measuring some non-commuting observables of the system by preparing and measuring the state multiple times [68]. The method is analogous to simpler examples, such as reconstructions of 3-dimensional objects by taking two dimensional projections of it along different Cartesian planes. This analogous two-dimensional projection method can be thought of as a reconstruction of an object by shining a light on it from different angles and detecting the shadows the object produces at certain angles. Then the 3D object could be reconstructed by compiling the information gained from the object's shadows.

Similarly to the real space analog, a certain number of projections is required to accurately reconstruct a quantum state. For our task of reconstructing the density matrix of a superposition spatial mode state, we need to measure a set of these identical states in multiple different MUBs and reconstruct the state from these measurements. When doing this we followed the procedure described in [50], for the same task. As already mentioned, since you affect the state when measuring it, the actual process requires multiple systems prepared into the same state, that are projected on different states in different MUBs. For reconstructing the full density matrix out of these measurements, there exist different methods of doing quantum state tomography, one of which is direct inversion. The direct inversion we are using here requires a measurement in all MUBs of the state space. This means that, e.g. for a prime-dimensional system, we have d+1 MUBs where d is the dimensionality of our selected section of Hilbert space [21]. This results in d(d+1) projectors $\Pi_m^{(k)} = \left|\phi_m^{(k)}\right\rangle\left\langle\phi_m^{(k)}\right|$, where k is the MUB number and m is the mode number. Thus, in order to perform the direct inversion on the quantum state we are measuring, it needs to be projected on all these m states in the k MUBs. If each of these projections produce a corresponding normalized detection rate $P_m^{(k)}$, the direct inversion for the density matrix can be calculated using

$$\hat{\rho} = \sum_{k,n} P_n^{(k)} \Pi_n^{(k)} - I, \tag{4.2}$$

where I is the identity matrix. This result is just a sample mean estimate of the density matrix, calculated from the multiple projections [68, 69]. The biggest problem with this method is the fact that it may produce states that don't correspond to a physical state, i.e. the Bloch vector is longer than one [68]. But the method is still preferred since it doesn't produce systematic errors and therefore gives the closest estimate of the density matrix consistently [70].

5 EXPERIMENTAL IMPLEMENTATIONS AND RESULTS

In the previous chapters we have introduced all of the tools needed for performing an arbitrary mode-conversions experimentally. The next step is then to implement the WFM mode-converter and test it. The first tests were on how this mode-converter can be used in spatial mode measurements. In the second tests we implemented multi-mode transformations, and built a heralded single photon source that we used in testing them. Finally, we tested the photon source in a regular HOM interference setup. Our light source, in the tests without single photons, was a continuous wave laser at 808 nm. For detecting the laser light, we used a simple photodiode power meter (Thorlabs PM1000D).

5.1 Mode filtering

In the First task we tested our WFM mode-conversions for mode filtering, i.e. projection on a single mode by filtering all other possible modes out. We chose this as an initial task because it is important in spatial mode communication applications, and it also gives a good estimate on our MPLC implementations accuracy and efficiency.

5.1.1 Implementation

To start off with, we required an input channel that we can use to generate different spatial modes. We realized this by using the amplitude masking method described in section 3.3. We first collimated our laser light out of an SMF and directed it towards an SLM. Then on the SLM we carved out the center of this big Gaussian beam and imprinted the wanted transverse structure on it. Next, we implemented the MPLC on a single SLM. To achieve this we placed a mirror 40cm away from the SLMs surface, and the mirrors surface was placed roughly parallel with the SLM surface. Then, with the correct gratings displayed on the SLM and with the correct beam input angle, the input light reflects off the SLM surface three times, with two reflections off of the mirror in between. A sketch of this setup can be seen in figure 5.1. Since the beam diffracts at three different locations on the SLM, we can display three consecutive phase-modulation screens on the same SLM. In this implementation, the beam propagates for 80 centimeters between the modulating screens and effectively we have an implementation of MPLC using WFM and a single SLM.

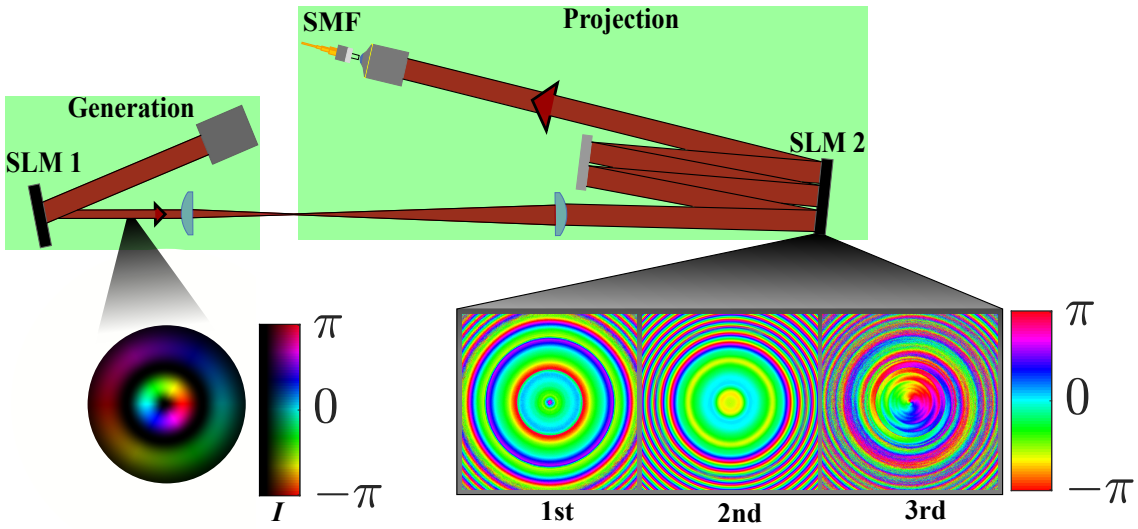

Figure 5.1. *The first configuration of our mode-converter setup. In this configuration any type of input beam can be created through amplitude and phase masking, then out this input state can be filtered onto any other state using three phase screens and a SMF. The phase screen structures are calculated using the WFM algorithm, and the modulated beam is coupled into a SMF after the phase screens. In this figure the beam is incident out of a SMF collimator and the two lenses after SLM1 enlarges the beam in order to increase the number of pixels used on SLM2 for the mode conversion. The coupling into the SMF at the end of the setup is done with a microscope objective. The example holograms (bottom right) convert a* LG_1^{-1} *mode (bottom left) into a Gaussian. The gratings that are added to the phase screens have been omitted for clarity of the figure. The colormap, again, describes the phase structure between different points on the beam or on the holograms and the intensity structure of the beam is shown by dimming the low intensity parts.*

In this implementation we chose to go with three phase-modulations and 80cm of propagation, because already three modulations with these distances seemed to work well in simulations. A bigger number of modulation-planes would've decreased the overall efficiency, due to the SLM losses, and a smaller number wouldn't have been sufficient for our conversions.

After our beam has gone through the converter, it is coupled into a SMF. As already discussed in section 3.3, a SMF can act as a Gaussian spatial mode filter. Hence, only light that has been converted into a Gaussian in the converter, couples in to the SMF. Since the mode-conversions generated using WFM are unitary, the orthogonality of different modes should be conserved in the converter. From this unitariness it follows that, if we only optimize our conversion for transforming a single spatial mode into a Gaussian, all modes that are orthogonal with it are orthogonal to the Gaussian after the mode-conversion. Hence, the combination of a SMF and a Gaussian mode-conversion effectively filters for any input mode we create the conversion for.

Between the mode generator and converter, the beam is enlarged using a two-lens telescope system (4f-system) that images the input mode onto our mode-converter SLM. The enlarged beam waist at the mode-converter is 0.94mm. This enlarging is done in order to make our beam mode big compared to the SLM pixels, since the pixel size ($8\mu m$) limits how accurately we can modulate individual parts of our beam. As a result, a bigger beam is modulated by more pixels giving the individual phase screens a better effective resolution. After the mode-converter, the beam is coupled

into the SMF using a microscope objective. This microscope objective is placed on a coupling stage on which we can adjust its position with high precision. We also placed two mirrors in front of the objective that we used to adjust the beams angle and position in the objective. The microscope objective we used had a $\times 20$ magnification. One additional parameter we adjusted during the mode-conversion was the beam waist. It was decreased during the conversion to 0.68mm, to match the beam waist of our SMF coupler.

There are a few additional details omitted from figure 5.1, in order to simplify it. In the mode-conversion we added blazed gratings the phase screens, which are not shown in the figure. This was done, since the SLM we use is only 70-75% efficient, hence the gratings separate the 25% of unmodulated light from the modulated light that we are interested in. Also, in the amplitude masking process, a pinhole is used at the focus of the 4f-system to separate the first diffraction order from the others. However, in the mode-converter this was not necessary since the long propagation distances separated the different orders sufficiently.

5.1.2 Results

We first tested this mode filter with some LG and HG modes. Out of these mode-families, the chosen test sets were the nine lowest order spatial modes of both families. We define mode order from the Gouy-phase multipliers, $2p + |l|$ for LG and $n + m$ for HG. We used the previously introduced 808nm laser for these measurements.

The measurements were done by carving out a specific LG or HG mode at the first SLM, and then filtering for another mode using our mode-conversion technique. In the measurements we performed all nine single state projection measurements on all nine input modes. But we did not perform projections on modes from different mode-families. Thus, the measurement accuracy was tested by comparing how much the wrong input modes seep through the mode filter. Meaning that if we project our input mode onto an orthogonal mode, nothing should be detected after the SMF. In contrast, if we project onto the input mode, the detected signal should increase dramatically. We then arrive at the crosstalk matrices in figure 5.2 a)-b), for LG and HG modes respectively. These matrices give information on how well each orthogonal mode pair can be distinguished from each other with this projection method, i.e. each column represents a setting on the filter and each row represents an input mode. Then, each matrix value tells the normalized rate of detected light with each combination of settings. The simulated conversions we used achieved a 99.9 % overlap between our converted modes and the wanted Gaussian mode, in simulations. This value is decreased due to the slight errors and misalignment's in the setup. The method we used for mode generation was not perfect either [49], and probably affected the measurement results. However, we still achieved SMF coupling efficiencies between 50-75 %, as can be seen in figure 5.2 c).

When comparing this projection method to a method built for the same task, e.g. intensity-flattening, the achieved efficiencies were better [50]. Another benefit of this method is that our losses seem to be mode order independent. Furthermore, if implementing the phase screens using refractive optical phase elements [58], or more efficient configurable devices, e.g. better SLM or

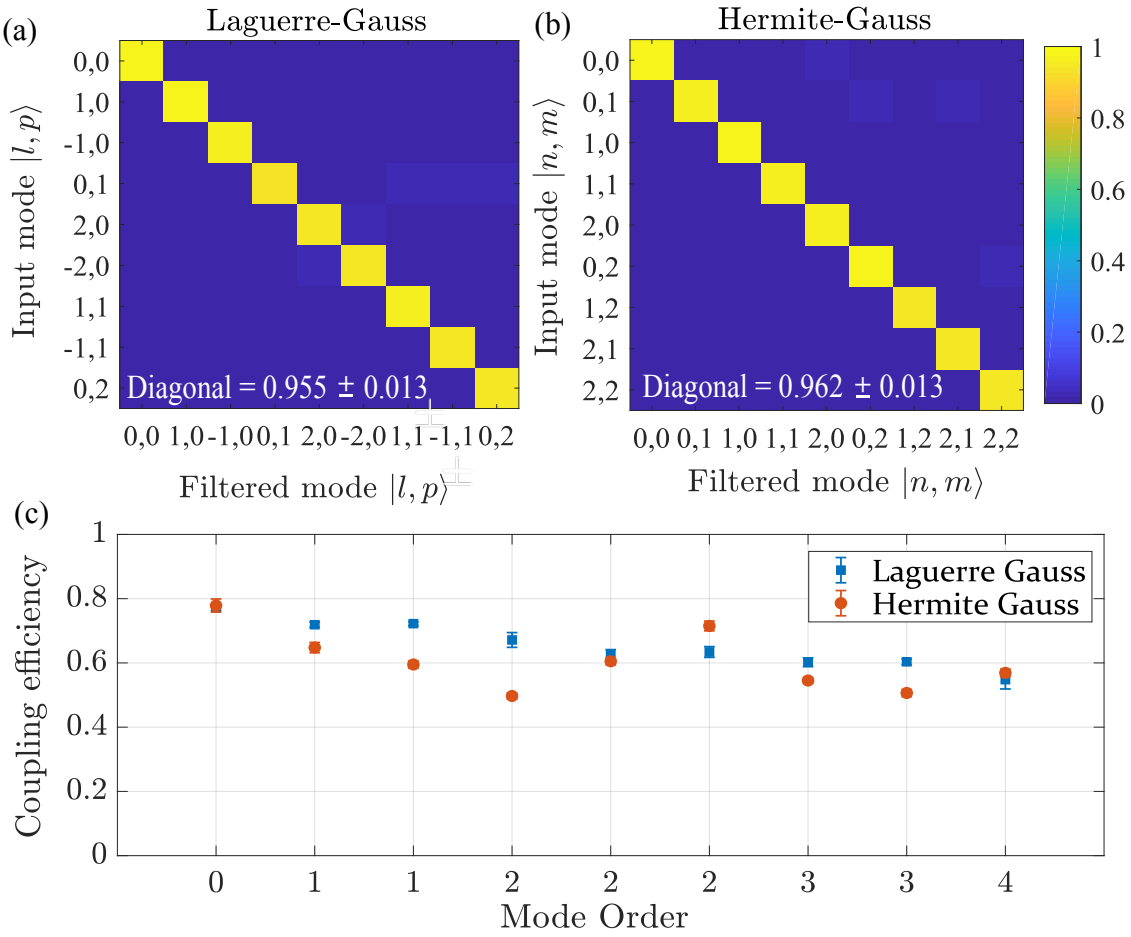

Figure 5.2. *Results from the mode projection measurements. a) shows a Crosstalk matrix between different LG-modes and b) shows the same for the nine HG-modes used. The y-axis of these matrices describes the mode going into the converter and the x-axis corresponds to the mode we are filtering for. This means that each element of the matrix tells us how much light is detected when we input a certain mode and use a certain projection on it. The values are normalized such that the values in each column sum up to one. The inlaid Diagonal values tell the mean and standard deviation of the values in the matrix diagonal. In c) we have plotted the coupling efficiencies into the SMF after the conversion, i.e. the efficiencies of the specific mode projections when the same mode is generated and measured. The modes on the x-axis of graph c) are in the same order as in figures a) and b).*

deformable mirror, the total efficiency of the implementation could be improved.

For characterizing the accuracy of the method, the modal crosstalk matrices need to be analyzed. Visibility is the most common figure of merit for the modal crosstalk, and is usually defined as

$$V = \frac{\sum_i C_{ii}}{\sum_i \sum_j C_{ij}}, \tag{5.1}$$

where values C_{ij} correspond to the crosstalk matrix elements. The visibilities achieved were 95.5 $\pm$ 2.4 % for the Laguerre-Gaussian modes and 96.2 $\pm$ 2.8 % for the Hermite-Gaussian modes.

Overall, the high visibilities in addition to high efficiencies mean that our mode-converter implementation is close to a perfect unitary conversion. This makes WFM mode-conversion potentially

useful in actual projection measurement experiments requiring high efficiencies. We will next test this applicability by using it in a QKD type measurements, and by performing a QST with it.

Quantum key distribution

In the first applied task, we measured the performance of our filter, if implemented in the high-dimensional version of the two-MUB BB84 quantum cryptography-protocol. As already specified in section 4.1, for testing the performance we needed to prepare and measure our photon states in two different MUBs. As our state space, we chose the seven LG modes $|\psi_n\rangle \in \{LG_0^0, LG_0^1, LG_0^{-1}, LG_1^0, LG_1^1, LG_1^{-1}, LG_2^0\} = \{|1\rangle, |2\rangle, ..., |7\rangle\}$. The indexing of the states is for simplifying the related figures. The required second basis set can be any MUB obtained from the linear superpositions

$$\left|\phi_i^{(k)}\right\rangle = \frac{1}{\sqrt{d}} \sum_{m=0}^{d-1} \omega_d^{(im+(k-1)m^2)} |\psi_m\rangle, \tag{5.2}$$

which is sometimes called the high-dimensional Hadamard transformation. In equation (5.2) $\omega_d = \exp(i2\pi/d)$ is a dimension dependent phase term, $k \in \{1,2,...,d\}$ are the different MUBs, i is the mode index in MUB k, and $|\psi_m\rangle$ are our set of chosen modes in our computational LG basis. With this transformation we can generate d modes in all the other d MUBs for any subspace with a Hilbert space of prime dimension d [17, 21]. The different MUBs are chosen by changing the value of k, but since we only needed one additional MUB for the QKD protocol, we chose $k = 1$, which is commonly referred to as the Fourier-basis.

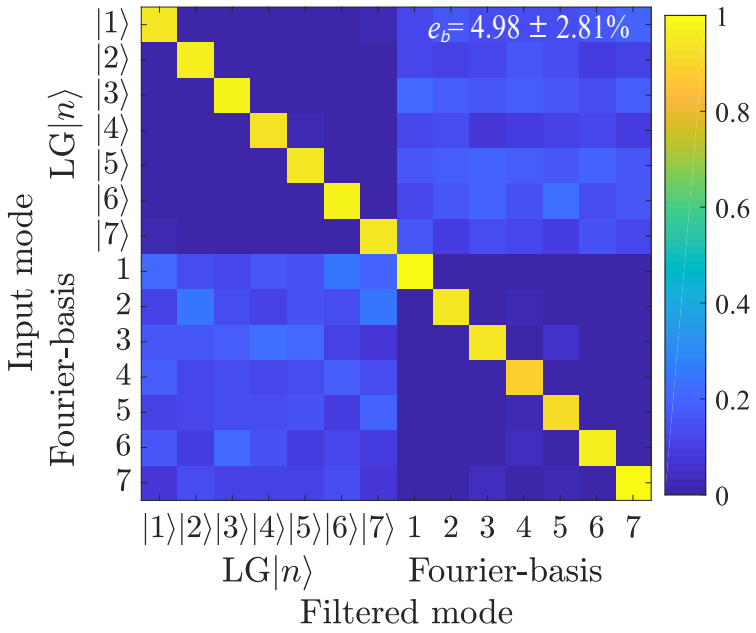

Figure 5.3. *Crosstalk matrix between two MUBs measured in order to evaluate our mode filters potential in a high dimensional QKD protocol. The projections onto modes from differing MUBs produced values close to the expected rate 1/d which is roughly 0.14 for the normalized results of our seven-dimensional subspace. The quantum bit error rate, which was calculated from the visibilities in both MUBs, is inset in the upper left corner.*

The important result that can be calculated from these filtering measurements is the secret key rate, which tells us how many secure bits of the key can be transmitted with one photon. We calculate the key rate for our sifted photons using the equation (4.1).

From our results shown in figure 5.3, we calculate an error rate of 4.98±2.85 %, corresponding to 1.98±0.39 bits per sifted photon. Which is almost twice the bit rate per photon achieved by using a more commonly studied two-dimensional state space. Additionally, the maximum error rate allowed by this 7-dimensional protocol is 23.72 % [67]. This means that the system can withstand more errors than a two-dimensional one. Of course, as already mentioned in section 4.1, with a filtering measurement, the losses in the system increase, resulting in a lower absolute transmitted bit rate.

Quantum state tomography

In the second task we performed a full quantum state tomography, as described in section 4.2. For this, we used the same set of seven LG-modes, as we used for the QKD measurements. But for this task, we created a superposition state, with a visually distinct density matrix, out of these seven modes. The state vector was of the form

$$|\Psi\rangle = \frac{1}{N}\sum_{n=0}^{6} \sin(\frac{n\pi}{6})\,|n+1\rangle\,, \tag{5.3}$$

where N is a normalization constant and $|k\rangle\,, k \in [1,7]$, are the used modes with the same indexing that was explained in the previous subsection. We projected the state onto every mode in the eight MUBs of our seven-dimensional state space. Meaning that we filtered the selected superposition

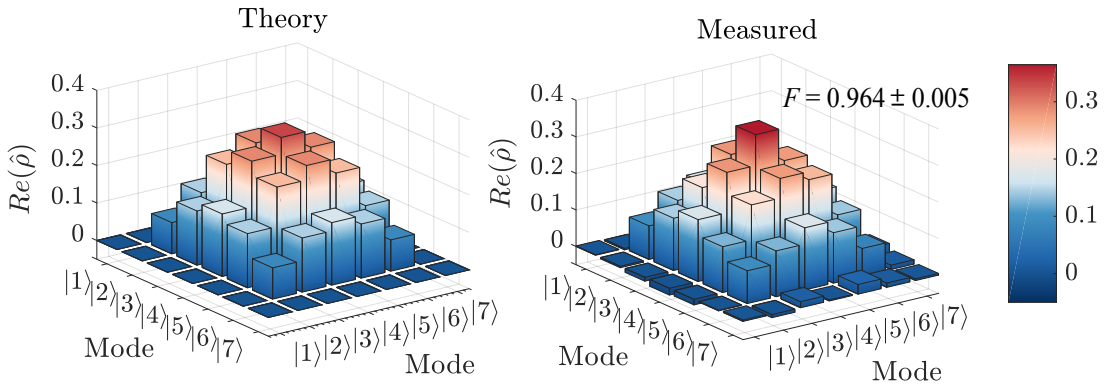

Figure 5.4. *Result of our quantum state tomography measurement. The two plots represent the real parts of the density matrices for the prepared state and the experimentally reconstructed version of it. The imaginary part is zero for the theoretical one and only has minor fluctuations for the measured one. The inlaid value in the upper right corner is the fidelity averaged between multiple repeated measurements.*

state through filters generated for all of the 49 modes calculated using equation (5.2), in addition to the seven LG-modes. The density matrix of the state is then reconstructed from these measure-

ments using equation (4.2). The theoretical and reconstructed density matrices can be found in figure 5.4.

A common figure of merit for the quality of the reconstruction is the state fidelity which is calculated by $F = \left(\mathrm{Tr}\sqrt{\sqrt{\hat{\rho}_{exp}}\hat{\rho}_{th}\sqrt{\hat{\rho}_{exp}}}\right)^2$ [71], where $\hat{\rho}_{exp}$ is the reconstructed density matrix $\hat{\rho}_{th}$ is the theoretical one and all of the square roots are matrix square roots. The fidelity of our measured state is 96.4±0.5 % which is quite a good accuracy, comparable to the fidelities achieved with the intensity-flattening method [50], proving the methods applicability in this task as well.

5.2 High-dimensional quantum gates

In the second set of experiments we wanted to be able to test conversions into modes other than the Gaussian. Furthermore, we wanted to test multiple different input and output modes for the same set of conversion holograms. This meant that we could use the same mode generation and conversion setups. But we needed to add a third SLM that does a mode measurement after the mode-converter. Thus, we moved the SMF coupling a bit further back and introduced a third SLM between the coupler and the mode-converter. A sketch of this setup can be seen in figure 5.5. The

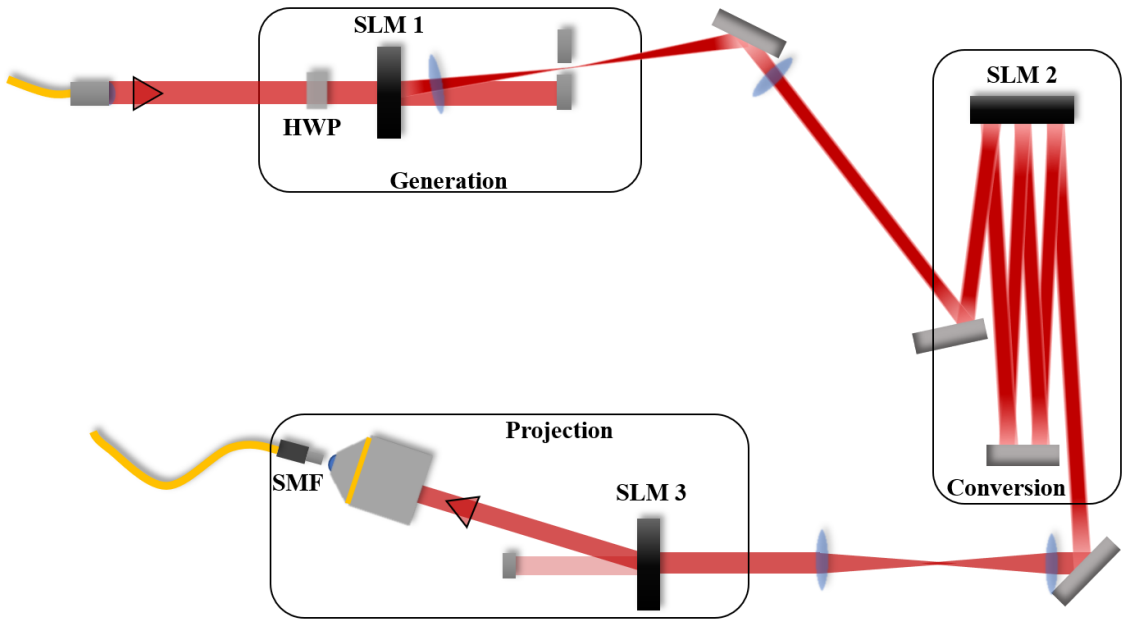

Figure 5.5. *Second configuration of our mode-converter setup. In comparison to the first configuration we've added an imaging system after the mode-converter and a third SLM before the SMF coupler for a separate mode filtering measurement. Meaning that we can generate any mode, do an arbitrary transformation on it, and project it onto any mode. The figure also shows the fact that we only use the first diffraction orders of the generation and measurement holograms.*

converted mode is again imaged onto the third SLM after the mode-converter using a 4f-system, and on the third SLM an intensity- or phase-flattening protocol can be performed to project onto any transverse-spatial field structure. These protocols are explained in more detail in section 3.3. With this setup we can now test multi-mode conversions, i.e. sets of phase screens that can trans-

form multiple different input modes into different output modes. Since all of these conversions would happen in the same beam path, we can use this setup to implement high-dimensional quantum gates. With quantum gates we mean devices that perform an input dependent transformation on all of the modes in our state space. An example of these kinds of conversions is the Hadamard gate shown in figure 3.1. What this two-dimensional Hadamard gate does, is convert our two orthogonal modes into different orthogonal modes in a separate MUB.

When using the intensity-flattening process on the third SLM, we again adjusted the beam size during mode-conversion. We reduced the beam size to 0.47mm, in order to have a good visibility in the final intensity-flattening measurement. The reason why we need to decrease the beam size in intensity-flattening was described in section 3.3. The clear benefit of doing all of these processes on SLMs is the adjustability. Because of this adjustability, we can very quickly change between different input modes, different conversions, and the modes we project on. The only disadvantage of our liquid crystal SLMs is the limited efficiency. Note that all of our SLMs were reflective and the transmissive SLMs drawn in figures 5.5 and 5.11 were only used to simplify the sketches.

5.2.1 Photon pair source

We also use single photons for half of these multi-mode conversion measurements. For this we required a heralded single photon source. We realised this source by generating a time correlated photon pair through SPDC and heralding the other photon using its pair. This photon pair can then also be used for two-photon interactions for example.

Our photon pair source (PPS) consists of a continuous-wave pump laser at 405nm, a type-II periodically poled (pp) nonlinear crystal made out of potassium titanyl phosphate (KTP), a band pass filter to filter out the pump laser, a polarizing beamsplitter to split our photon pairs and a stage to control the temporal overlap of our photon pair. A simplified sketch of the PPS can be found in figure 5.6.

The periodically poled (quasi-phase-matched) nonlinear crystal is where we generate the photon pair. The used ppKTP crystal has a change in the crystal structure after every $\Lambda = 10\mu m$, which allows QPM to happen for SPDC with an input wavelength around 405.28 nm and a degenerate output of two photons at around 811.1 nm. The bandwidth of our pump laser was 6 pm and that resulted in a 1.2 nm down-conversion bandwidth. We also tested the down-conversion with a similar pump laser, which had a 1.8 nm pump bandwidth. However, we changed to the narrower pump laser due to problems we will discuss later. This QPM was designed for collinear operation and optimal type 2 phase-matching. The phase-matching was tuned by changing the crystal temperature to 54.5°C. The optimal temperature is dependent on the exact laser wavelength and the specific crystal used, due to the phenomena discussed in section 2.2.2. In order to control the crystal temperature, the crystal was placed into an electrically controlled small oven, with a temperature sensor and an aperture for shining light into the crystal. Additionally, since the efficiency of the crystal is dependent on the pump beam polarization (see section 2.2.1), a half-wave plate was placed before the crystal, and oriented in a way that maximizes the SPDC output power from

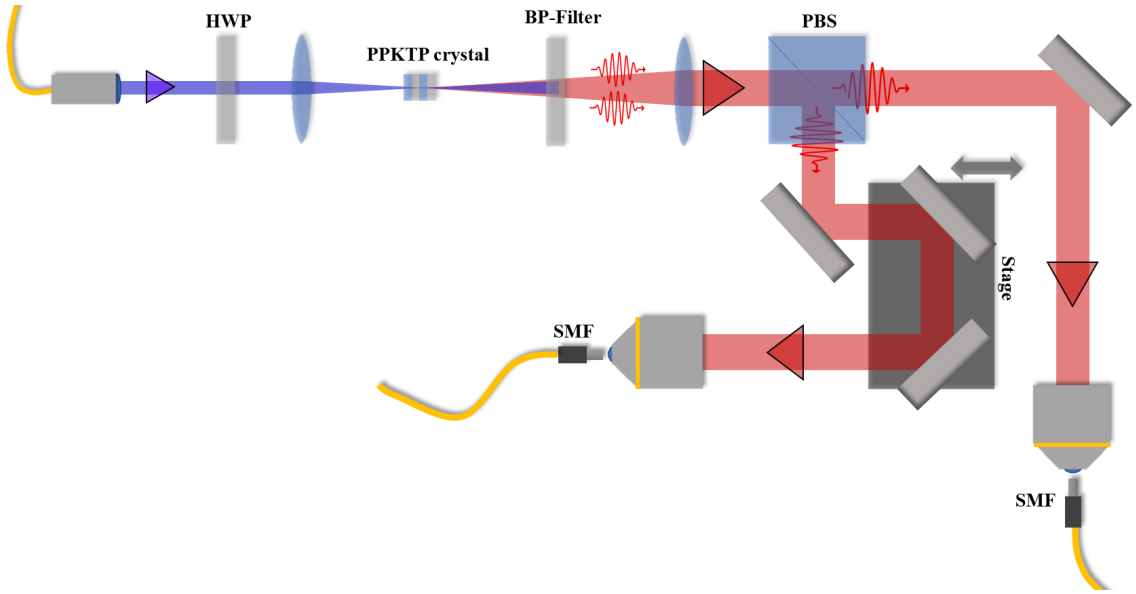

Figure 5.6. *The photon pair source used. In this figure the pump beam of around 405nm is represented by the dark purple color and the down-converted 810nm photon beams are in red. The components shown are a half-wave plate (HWP), the nonlinear crystal (PPKTP), a band-pass (BP) filter for 800±20nm, a polarizing beamsplitter (PBS) and a translation stage. First the pump beams polarization is adjusted with the HWP and it is focused in to the crystal. Then the pump is filtered out with the band pass filter, the photon pair is collimated with a second lens and the photon pairs are split with the PBS into two paths, depending on their polarization. Then the path length travelled by one photon is adjusted by moving the two mirrors on the translation stage. Finally, both photons are coupled into single mode fibers (SMF) with microscope objectives.*

the crystal. Finally, the last component maximizing the crystal output power were the lenses. By changing the focal lengths of the two lenses, one focusing into the crystal and one collimating the light after the crystal, we can change the achieved output power. These focal length changes effectively change the pump beam waist, and the waist of the beam we collimated out of the crystal. Then, by changing the relation of these two, we change the number of different spatial modes that we have in our down-converted beam [72]. This then changes our overall power since we are coupling the down-converted photons into single mode fibers that only couple in a single spatial mode. The focusing lens was a 200 mm focal length lens with an ultraviolet anti-reflection coating and the collimating lens had a focal length of 50 mm with a near-infrared anti-reflective coating.

After our optimization of the SPDC power, we still needed to separate all of the photons from their partners. Also, while doing this we need to preserve the exact time correlation the photons got from being born in the same SPDC process. Since we are using a type 2 crystal, we can separate the photons with a polarizing beamsplitter (PBS). This orthogonality in polarization means that we can separate the pair with almost a 100% efficiency, with the upper limit being the efficiency and absorptiveness of our PBS. This easy separation of the pair is the main advantage of type-II phase-matching for us. Next, we conserve the temporal correlation by trying to keep the optical lengths of the two paths the same from the PBS into each of our fiber couplers. Of course, human error in length measurements, and deviations in fiber lengths, will cause changes in the path lengths. Thus, we also introduced a delay line, with two mirrors (see 5.6), that can be used to adjust the path

length in one of the arms. This allows us to scan the path lengths and then perfectly temporally overlap our photons.

Finally, we couple the photons into single-mode fibers by putting the SMFs behind microscope objectives on stable and easily adjustable coupling stages (stages not shown in figure 5.6). The microscope objectives used here had a $\times 10$ magnification As in the previously described setups, the couplers had two mirrors in front of them, that were used to change the input position and angle of the photon beams entering the coupler. Also, as previously mentioned, the SMF coupling filters in only one spatial mode. This spatial mode filtering guarantees that, at the other end of the fiber we have a perfect Gaussian mode on our single photons.

Some additional considerations for the focusing and collimating lenses come up when we want to keep our two photons indistinguishable. For example, adjusting the waist size and position for the collimating lens can change the time delay spread between the two photons [73], but at least for long coherence length pumps, this shouldn't affect the indistinguishability of the photon pair [30]. This time delay spread can be intuitively understood by considering the spread of locations, where the photon pair could be formed. Then, due to the birefringence and the orthogonal polarizations between the two photons, the delay between them changes depending on the distance they have to travel through the birefringent crystal. But this spread shouldn't affect the interactions between the pair, with our narrower bandwidth, long coherence length pump laser. But with the initial broad bandwidth pump laser it was noticeable. Additionally, these focusing parameters can affect the spectral profile of our down-conversion [73, 74, 75], which might also affect the spectral distinguishability of our two photons. When building the PPS in question, these lens combinations weren't considered much, since sufficient power was achieved just by matching the beam waists of the focusing and collimating lenses.

Lastly, for our single photon measurements, we required more sensitive detectors. The single-photon detectors we used were avalanche photodiodes (APD) with a fiber input. These APD detectors (Laser Components Count T) are designed to have a huge current gain from a single photon absorption, due to the big reverse bias. Two of these APD detectors were used for the photon pairs, and the detection signals were fed out of them into a time tagger module (TTM8000). This time tagger then labels the detection times of each photon such that a computer program can distinguish which photons were detected at the same time. With these simultaneous detections, or coincidences, we can herald a single photon, as already discussed in section 2.2, or measure the behaviour of a photon pair in bi-photon interactions. These simultaneous detection events have a certain detection window (here 0.5 ns to 1 ns) in which two detections are deemed to be simultaneous, due to the temporal accuracy of our detectors. Therefore, we can only trust the coincidences to signify pairs if the rate of detected single photons compared to this coincidence window is small, and if the signal to noise ratio is sufficiently low in the APD detectors. Fortunately, the dark count level of our APDs is roughly 30 erroneous detections per second, which translates to roughly a 3×10^{-8} chance of a photon being detected in a 1 ns time window. Correspondingly the probability of an accidental coincidence out of these dark counts is the square of this value 9×10^{-16}. If we additionally keep our single photon rates at MHz, or below, the chances that two photons accidentally coincidence is improbable compared to the rate of actual pair detections.

5.2.2 Results

We implemented two different high-dimensional quantum logic gates for different sets of LG-modes. For the first gate we still used the same 808nm laser but for the second one we used our heralded single photons.

The first gate we implemented was an X-gate. In short, a high-dimensional X-gate or NOT-gate cyclically shifts the bits [14]. In a two-dimensional case this means that a 1 becomes a 0 and a 0 becomes a 1. However, in our chosen three-dimensional basis, LG_0^{+1} converts to LG_0^0, LG_0^0 converts to LG_0^{-1}, and LG_0^{-1} is converted to LG_0^{+1}. Note, that a method of implementing OAM-mode X-gates is already known, but the WFM method can be extended to full-field spatial mode X-gates, which we showed in a related article [17]. A more general definition of high-dimensional X-gates can be found in [14], where a different method of constructing OAM-mode X-gates is also shown.

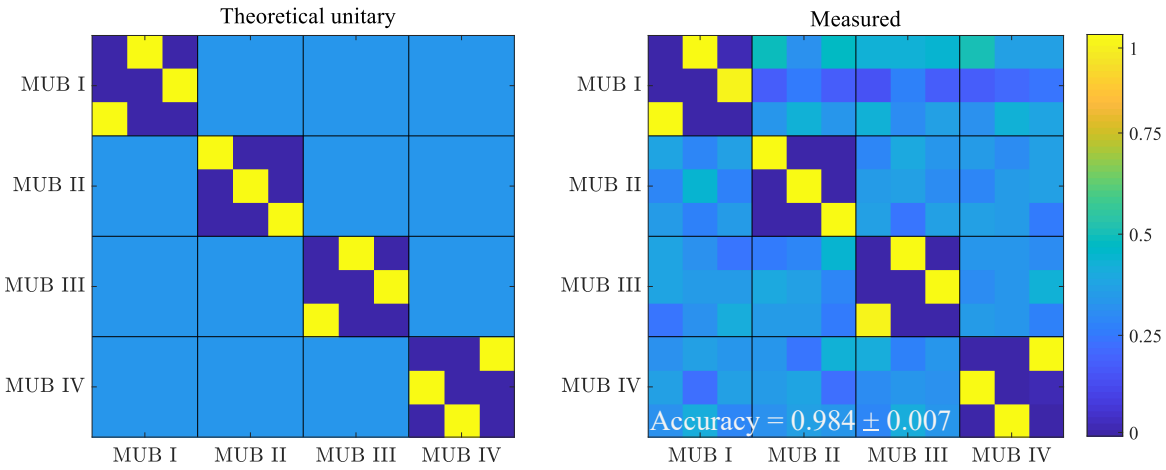

Figure 5.7. *Crosstalk matrix of the three dimensional X-gate for the set of LG-modes LG_0^1, LG_0^0 and LG_0^{-1}. The behaviour of the gate was measured in all MUBs to measure the unitarity of the transformation, from the accuracy and phase stability of the conversion. The inset accuracy is the mean and standard deviation of the matrix values with the yellow colormap values. The MUB indices are in the order of the k-indices in equation (5.2) with $k = 1$ being MUB II and MUB I being the LG-mode basis.*

The measured conversion accuracies are shown in the crosstalk matrix of figure 5.7. The crosstalk matrix values here are calculated in the same way as before In order to examine the true unitarity and usefulness of the gate, the measurements were done in all four MUBs of our three dimensional basis. From the combined results of the gates operation in all MUBs we can infer the unitarity of the gate. This means that for a truly unitary transformation we should have a lossless and repeatable operation of the gate in all MUBs. Or in other words, in all MUBs the mode orthogonality should be conserved, and no losses should occur. Our implementation is nearly unitary, with only minor alignment errors etc., as can be seen from the crosstalk matrix in figure 5.7. The unitarity of the process can also be investigated through quantum process tomography, that was done for these measurements in [17]. From this tomography we achieved a process purity of 99.3%, which is close to the 100% purity of a perfect unitary process. Also, a similar value to the previously

Input-mode indices		Output-mode indices	
l	p	l	p
+1	0	+1	0
-1	0	-1	0
+1	1	-1	1
-1	1	+1	1

Table 5.1. *A table describing the operation of our CNOT-gate. The gate changes the modes l-index if the p-index is 1. If $p = 0$, no transformation is done.*

shown “Diagonal"-values can be calculated for these results. We call this value accuracy and define it as a mean of the crosstalk matrix values shown in yellow in the theoretical crosstalk matrix of figure 5.7. The total achieved accuracy for conversions in all MUBs was 98.4±0.7 % for this OAM-mode X-gate.

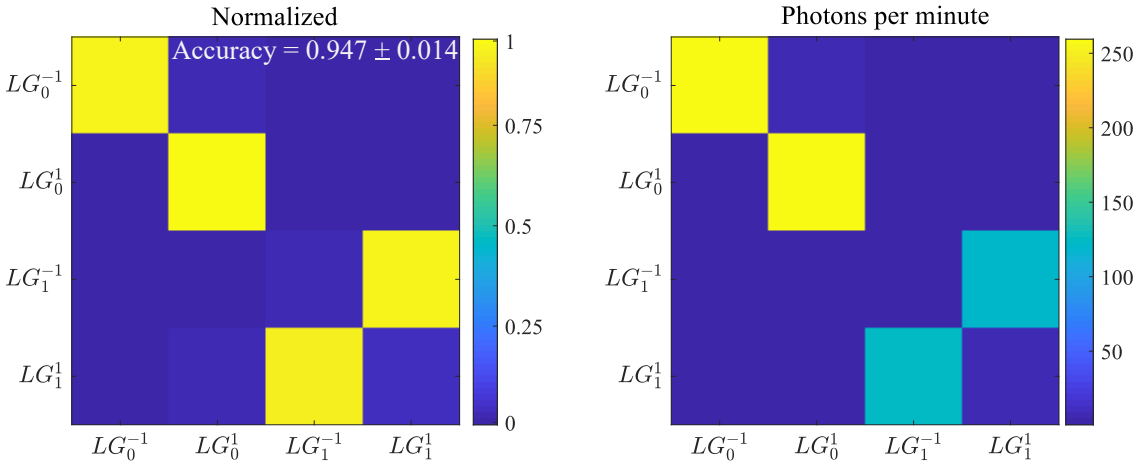

Figure 5.8. *A single photon CNOT-gate using full field LG modes. The gate works for the four LG-modes LG_0^{-1}, LG_0^{+1}, LG_1^{-1}, and LG_1^{+1}. If the input mode has a radial index of one, the mode is converted to the same mode of opposite azimuthal index. Conversely, no transformation is performed if the radial index is zero. The accuracy is defined the same way as in figure 5.7 and in the rightmost figure we show the averaged single photon values without normalization.*

The second gate we implemented was a type of controlled NOT gate (CNOT) for the internal degrees of freedom of a single photon. For measuring this gate, we used our heralded single photon source. The way our CNOT-gate works is that it uses one degree of freedom from our spatial mode quantum states to determine if a cyclic shift should be done in the other degree of freedom. The modes used here were LG_0^{-1}, LG_0^{+1}, LG_1^{-1}, and LG_1^{+1}. For our modes the CNOT-gate shifts a modes azimuthal index from minus one to plus one or vice versa, if the radial index is one. Then conversely, if the radial index is zero, no shift occurs. Effectively then, the radial index controls the NOT-operation. A simple table on the operation of our CNOT gate is shown in table 5.1 The results measured for this gate, with heralded single photons, can be found in figure 5.8.

The accuracy was a bit lower for these conversions, 94.7±1.3 %. This slight decrease in accuracy was probably due to multiple reasons. First of which is that this gate was optimized for

more modes than before. Secondly, the radial structure is included in these transformations, which makes the transformations more complex. Lastly, the spectral profile of our heralded single photons is a bit broader compared to our laser. The spectral profile's effect on our conversion accuracy is due to the alignment's wavelength dependence. This wavelength dependence comes from the fact that we display multiple diffraction gratings on our SLMs. Figure 5.8 also shows the number of heralded single photons we detected during our integration time of one minute per each input and output mode. The total observed losses were about 99.97% when comparing rate before the mode generation and at the single photon detection. This was expected though, due to the losses in the amplitude masking methods and all the SLMs.

5.3 Hong-Ou-Mandel interference

The final experiment we performed was testing our photon pairs in Hong-Ou-Mandel interference. During this process we tested multiple pump lasers for our PPS before ending up on the 6 pm bandwidth laser listed in section 5.2.1. While testing these different pump lasers, we observed a single photon rate of roughly 0.9-1MHz for 50mW of pump power. This rate is the average photon rate between our two SMF outputs in the PPS. The important factor is how many of these single photons per arm were part of a time correlated pair. This ratio of coincidences to singles varied between 20-48%, with 48% being the value achieved with the narrow bandwidth pump laser. So, for the coincidences, we had roughly a rate of 9120 Hz/mW, depending on the pump power.

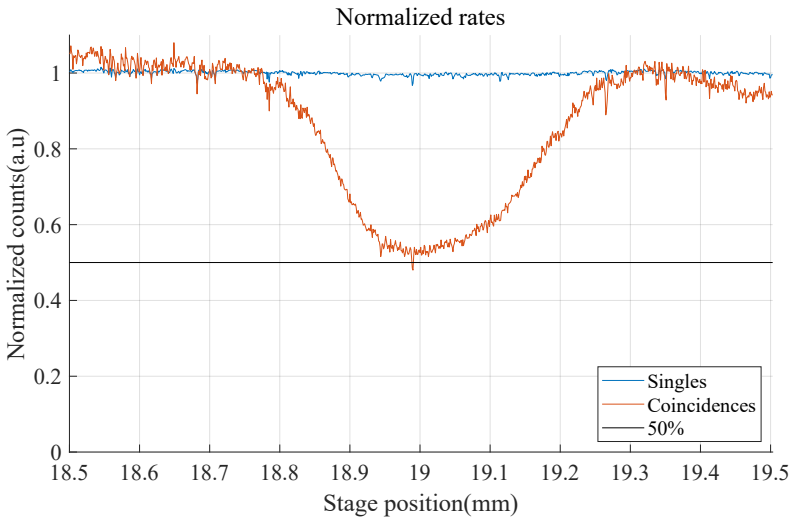

Figure 5.9. *Initial HOM interference result in a fiber beamsplitter. The measured visibility was* 0.478 ± 0.017*, which already indicates two-photon interference but doesn't exceed the limit that can be achieved by interfering more classical states of light (0.5) [76].*

This testing of different pump lasers in our PPS was done due to the non-optimal properties of our photon pair. By the quality of the photons we refer to the indistinguishability of the pair. This indistinguishability was tested by measuring the pairs HOM interference visibility in a fused fiber beamsplitter, and as already discussed in section 2.3, the better the visibility, the more repeatably we are generating indistinguishable photon pairs.

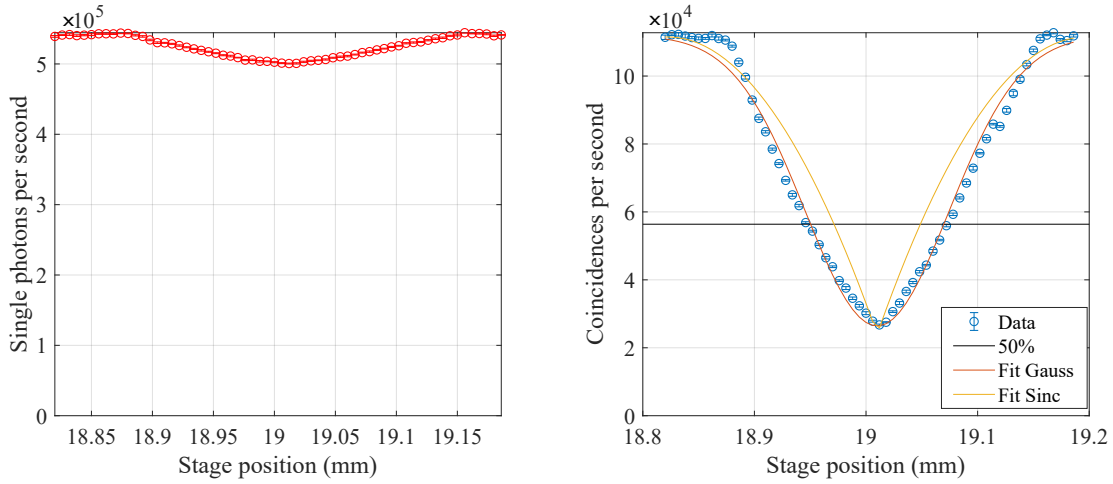

Figure 5.10. *HOM interference result in a fiber beamsplitter using the 6 pm bandwidth pump laser described in section 5.2.1. Two types of theoretical coincidence curves were tried to fit into the data with limited success. The fitted curves represent interference of photons with a Gaussian and a Sinc spectral profiles. The achieved visibility was* 0.760 ± 0.005 *calculated with equation (2.34). The left figure represents the simultaneously measured rates of single photons averaged between the two detectors. We can see a decrease in singles in the interference area caused by the fact that our detectors can only resolve one photon at a time. This means that when the photons start to bunch into pairs, the number of temporally overlapped pairs going into both detectors starts to increase. The expected decrease in single photon detections should then be half of the decreased coincidence values as is observed in our measurements (dip is roughly 80 000 coincidences deep and singles decrease by roughly 40 000 counts).*

The HOM interference visibilities were measured by scanning the translation stage over the position of zero path difference between the two photons. Thus, for perfectly indistinguishable photons with Gaussian spectral distributions, we should achieve similar results to the theoretical curves presented in figure 2.5. As mentioned in section 5.2.1, our first laser had a 1.8 nm bandwidth, and as can be seen from the related HOM results in figure 5.9, the dip in coincidences isn't as deep as it should be. Also, the width of the interference area is a bit broader than we would expect. This is most likely due to the differences in spectral distributions, caused by polarization dependent processes in our SPDC crystal (as discussed in section 5.2.1), and the possible variations in the time delays of the pairs. The visibility of this dip, calculated according to equation (2.34) was 0.478 ± 0.017. The value P_{CL} was the average coincidence rate outside of the interference area and P_{QM} was the coincidence rate at the lowest point of the interference area. The two aforementioned reasons can cause this spread and decrease in visibility, since if all of our photons are not fully indistinguishable spectrally and temporally, all of the photon pairs won't interfere. Also, if the time delay between the photon pairs varies, all the pairs won't interfere at the same stage position of the delay line. Hence, we would get a more broader interference pattern due to the spread of the photon pair delays.

With a narrow bandwidth laser, like the 6 pm bandwidth laser we introduced in section 5.2.1, these problems are reduced, and a higher visibility can be reached. The difference can be seen in figure 5.10 which was measured with this laser. Now the visibility was 0.760 ± 0.005, calculated with the same method as previously. However, now we included the experimentally calculated FBS

splitting ratio into the visibility. This splitting ratio just increased the value of P_{CL} by a factor of 1.0048. The visibility still wasn't perfect, and we suspect that the spectral distinguishability of our photons might still be an issue. The fit curves shown in figure 5.10 were adopted from [42] and [41].

One additional observation was a decrease in the single photon rates when HOM interference was observed. This decrease can be seen in the single photon rates in figure 5.10. The decrease is caused by the fact that our detectors are not photon number resolving. Hence, when our photons start to exit the FBS together, a greater number of these temporally overlapped photons enter the same detector, which counts the pair as only a single photon. From this we expect a decrease in single photon rates that is roughly half of the decrease in coincidences, since the single rates we show are an average rate between the two detectors. The exact two photon detection efficiencies of our detectors might cause small changes to this value. But the measured decreases did match this expectation quite well, since the single photons per detector decrease by roughly 40 000 counts/s when the coincidences decrease by about 80 000 1/s.

5.3.1 Setup for two-photon interference in transverse spatial modes

Finally, we constructed a third setup around our mode-converter. This time, the goal was to observe the two-photon interference effects in spatial modes, as discussed in section 2.4.3. The actual implementation of this setup is in principle, just the configuration shown in figure 5.5 with two inputs and outputs. A sketch of this setup is shown in figure 2.9. More specifically, in the setup we send two photons onto the first SLM, where we can carve two different transverse modes onto them using the familiar amplitude masking technique. We use a single SLM for multiple operations by directing the two photons onto different regions of the SLM and displaying two different holograms. After the spatial mode structures have been imprinted on the beams, they are overlapped with a beamsplitter. This overlapping loses half of the power from both inputs but it's the most flexible way to overlap the two photons. Once the photons have been overlapped, we perform simultaneous mode-conversions on both. This single beamline operation is necessary for the photon pairs to interfere, since our photons need to be indistinguishable in all other degrees of freedom. Of course, they can't initially be indistinguishable in the spatial mode degree of freedom, if we want to perform different mode-conversions on them.

After the two inputs are combined into a single beam, the mode-converter works the same way as before. Only now, two of the multiple inputs and outputs of the conversion can be utilized simultaneously. After the conversion we need to measure the transverse-spatial structure of the two output photons. This requires us to split the overlapped photon pair back into two different channels. We achieve this task also with a beamsplitter, but again, since this is a probabilistic method, only 50% of our photon pairs get separated. After this separation of our photons from their partners, we use different regions of the third SLM to do separate single spatial mode projections on the photons.

As can be seen from figure 2.9, both of the input channels are imaged from the first SLM onto the

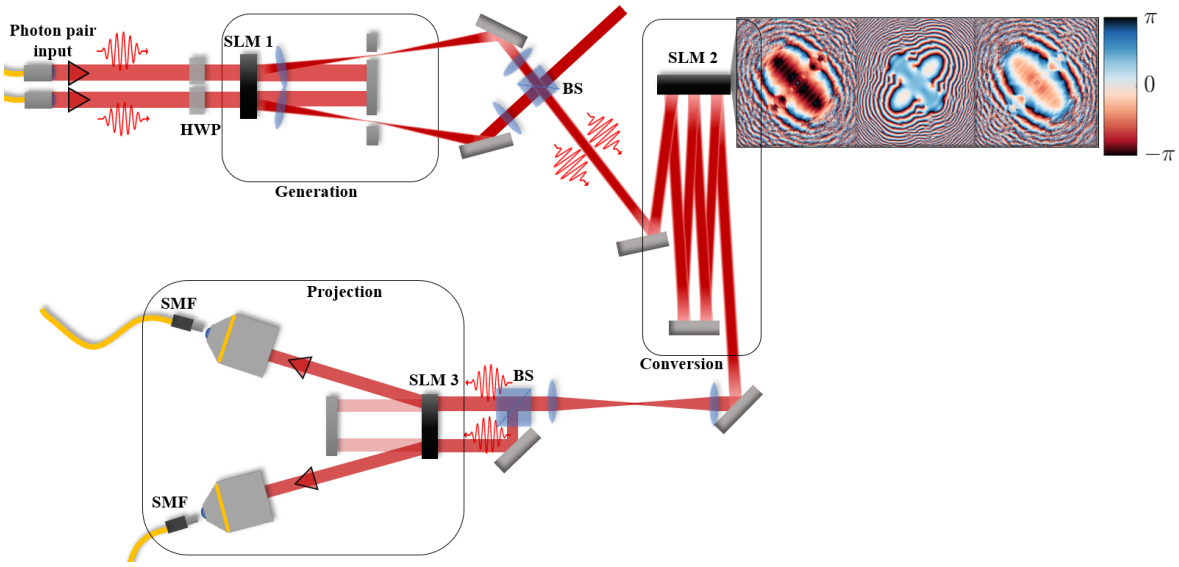

Figure 5.11. *Two-photon mode-conversion setup. In this setup we have two single photon inputs, which can be prepared into any spatial modes with SLM1. The single photons are brought into the system by SMF's from the photon pair source. These two channels are then spatially overlapped by a BS and directed onto the mode-converter. The mode-converter output is then split probabilistically by a second BS in to two paths. The two photons are then guided onto SLM3 for two separate projection measurements characterizing the correlations between the mode structures of the photon pair. There is a 4f imaging system between each SLM, and the imaging between SLMs one and two magnifies both of the input beams similarly. The inset mode-conversion phase screens in the upper right corner performs the unitary transformation described in equation (5.4).*

second one using a magnifying 4f-system. Similarly, the converted beams are imaged from the output plane of the mode-converter onto the third SLM by a simple non-magnifying 4f-system. The imaging is done to preserve the beam sizes and to avoid any spread of the mode-structure during propagation.

As we already mentioned, this setup is mainly for testing two-photon interactions in simultaneous unitary spatial mode conversions. The initial task with this setup would be to observe HOM interference in the spatial mode degree of freedom instead of the usual path degree of freedom. In effect, we are now able to realize the beamsplitter-like mode-converter detailed in section 2.3, i.e. a Hadamard-gate between different spatial mode MUBs. Following these two-dimensional tests, studying two-photon interference in a higher-dimensional state space would be easily achievable with this same setup. These higher dimensional state spaces would only require a different mode-conversion, e.g. a three-way beamsplitter (tritter) for a three-dimensional state space [77].

We haven't had time to test this setup yet, but we have constructed all of its parts, and are almost ready to test it. The initial test would be implemented using the LG_0^{+1} and LG_0^{-1} modes, since they are efficient to detect with the phase-flattening technique. The mode-conversion, shown in figure 5.11, is the most efficient Hadamard-type conversion we found for these two modes.

$$\begin{bmatrix} |1\rangle \\ |-1\rangle \end{bmatrix} \longrightarrow \frac{1}{\sqrt{2}} \begin{bmatrix} 1 & 1 \\ -1 & 1 \end{bmatrix} \begin{bmatrix} |1\rangle \\ |-1\rangle \end{bmatrix} = \hat{U} \begin{bmatrix} |1\rangle \\ |-1\rangle \end{bmatrix} = \begin{bmatrix} \frac{1}{\sqrt{2}}(-|+1\rangle_d + |-1\rangle_d) \\ \frac{1}{\sqrt{2}}(-|+1\rangle_d + |-1\rangle_d) \end{bmatrix}. \tag{5.4}$$

To use this unitary transformation in two-photon interference, we need to prepare one of the photons in a LG_0^1 state and the other in a LG_0^{-1} state. Then our otherwise indistinguishable photons should bunch into the same spatial mode in the mode-conversion. This bunching could then be observed as a coincidence decrease or increase, depending on which states we project the photons on at the last SLM.

6 CONCLUSION AND OUTLOOK

During this thesis, we set out to investigate, how a recently discovered MPLC technique called wavefront matching can be used to implement unitary transformations of spatial modes. We investigated its applicability in multiple different tasks with our final goal being two-photon interference. Since WFM is a purely computational method for transforming transverse structures of light beams, we first needed to define the input and output light fields between which we wanted to convert the beams and adopt the method for our specific use cases. In this thesis, we have explained how the WFM algorithm works, along with some underlying theory behind the quantized spatial modes, which we want to manipulate. After this we tested the method in a unitary spatial mode filter, and as an arbitrary multi-mode converter.

The results we measured demonstrate the versatility, flexibility, and efficiency of WFM. In the initial mode filtering (i.e. single state projection) tasks, we observed a good accuracy and high efficiencies in the conversions. We additionally tested the mode filters efficiency in quantum key distribution and in quantum state tomography. The filter worked well in both tasks, achieving a secret key rate of almost 2 bits per photon and a measured state fidelity of 96.4%. In contrast to other techniques relying on losses, e.g. intensity flattening [50], our technique's high efficiencies make it optimal in e.g. single photon tasks that require high efficiencies. The total efficiency of this implementation could be further improved, e.g. with refractive optical elements [58]. Of course, more efficient SLMs or deformable mirrors, with higher resolutions, would also improve the overall efficiencies. Additionally, if we can improve the efficiencies of these programmable devices, we wouldn't need to sacrifice flexibility over efficiency. On the algorithm side, imposing different restrictions on the simulated mode-conversions might make the whole process much more accurate and efficient. These algorithmic restrictions could, for example, be on the operation order (e.g. phase singularity removal in the first phase screen) or on the resulting structures on the holograms (e.g. smoother variations between phase values on adjacent pixels). Both suggestions could help with the systems alignment and improve the conversion efficiencies, but this needs to be investigated in more detail. Furthermore, investigating the effect of different propagation distances in the conversions might be beneficial, since these propagation distances between the phase screens should be connected to the achieved change in the transverse amplitude structure of light beams. However, these propagation distances should also be linked to the beam size, the number of modes in the transformation, and the number of phase screens. The reasons for this are the connection of the Rayleigh range to the beam size, and the fact that simultaneous conversions of multiple modes require more complex transformations [17]. As a result, investigating the propagation distance has a lot of other parameters that need to be controlled during further investigations.

The second part of our measurements showed that our implementation of mode-conversion by WFM is capable of handling multiple input and output modes in a single beamline. We demonstrated that with WFM we can simulate and implement different high-dimensional optical quantum gates and showed the unitarity of a three-dimensional gate. Additionally, we demonstrated that the gates also work with single photons by implementing a CNOT-gate for single photons. The way we implemented the CNOT-gate took advantage of the multiple internal degrees of freedom of a single photon. These high-dimensional internal properties of photons could be harnessed in new types of quantum computation schemes that don't necessarily require multiple quantized particles interacting with each other. Moreover, when combining the high-dimensionality with multiple particles we can achieve even larger Hilbert spaces. Overall, we only showed a few examples of high-dimensional computational gates that are possible to implement with WFM. Hence, there is many more unexplored possibilities with this implementation of optical quantum gates. In comparison to earlier spatial mode quantum gate implementations, such as the ones explored in [14], WFM implementations don't require multiple beam paths or interferometers. Hence, they are simpler to build. The lack of interferometers also make our implementations much more stable. In addition, since WFM can transform amplitude structures and phase structures, all transverse-spatial degrees of freedom can be included. This is in contrast to the previously known optical quantum gates [14], that rely only on the OAM-modes. The inclusion of full-field spatial modes enables new possibilities, like the CNOT, in addition to a higher-dimensional state space. However, the efficiency of this method still needs to be improved in order to make these devices usable in actual computational schemes. Additionally, there needs to be a way of integrating these conversions to smaller devices, if they are to be used in applications. All in all, these results, along with the additional results shown in [17], show the potential WFM has in producing unitary high-dimensional quantum gates for qudits.

In the last section of our experimental implementations, we built and simulated all of the parts needed for observing a two-photon interference in the transverse-spatial degree of freedom. However, even though the mode-conversions worked excellently, due to the limited time span of this thesis, we weren't able to optimize the photon pair source to the required level. We did observe a clear signature of two-photon interference, i.e. below the classically possible limit, but not at a level required for the subsequent tasks. Hence, our photon pair source needs to be further optimized, in order to observe a truly quantum interference in the spatial mode degree of freedom. We also listed some possible methods of improving the indistinguishability of our photon pairs. Implementing these changes is the obvious next course of action. One additional possibility for improving the indistinguishability of our photon pair would be to use a type 0 or type 1 phase-matched nonlinear crystal since then the effects caused by birefringence discussed in section 5.2.1 will not affect the pairs. After this initial two-photon interference is observed with the simplest transformation, i.e. only using two spatial modes, it will be interesting to move onto higher-dimensions, i.e. involving more than two modes, and more complex interferences. Additionally, similarly to the NOON states mentioned in section 2.3, this interference phenomenon could be used to entangle the photon pair in their transverse-spatial degree of freedom.

In summary, we demonstrated the applicability of WFM in multiple different quantum information applications such as, filtering, QKD, state tomography and quantum gates. The method also has

potential in more complex spatial mode transformations such as two-photon interference schemes, or as an entangling gate. We also tested the unitarity of these transformations and showed that our implementations were close to perfect unitaries. This ´´unitariness" is especially important since it preserves coherence and orthogonality of our photon states. We also constructed a novel two-photon interference setup and demonstrated the functioning of all the required parts. Thus, the obvious next step is to finalize the source, in order to observe this novel type of quantum interference, building on the presented preliminary results.

REFERENCES

[1] S.-K. Liao, W.-Q. Cai, W.-Y. Liu, L. Zhang, Y. Li, J.-G. Ren, J. Yin, Q. Shen, Y. Cao, Z.-P. Li et al. Satellite-to-ground quantum key distribution. *Nature* 549.7670 (2017), 43.

[2] C.-Z. Peng, J. Zhang, D. Yang, W.-B. Gao, H.-X. Ma, H. Yin, H.-P. Zeng, T. Yang, X.-B. Wang and J.-W. Pan. Experimental long-distance decoy-state quantum key distribution based on polarization encoding. *Physical review letters* 98.1 (2007), 010505.

[3] A. E. Willner, H. Huang, Y. Yan, Y. Ren, N. Ahmed, G. Xie, C. Bao, L. Li, Y. Cao, Z. Zhao, J. Wang, M. P. J. Lavery, M. Tur, S. Ramachandran, A. F. Molisch, N. Ashrafi and S. Ashrafi. Optical communications using orbital angular momentum beams. *Adv. Opt. Photon.* 7.1 (Nov. 2015), 66–106. DOI: 10.1364/AOP.7.000066.

[4] C. A. Brackett. Dense wavelength division multiplexing networks: Principles and applications. *IEEE Journal on Selected Areas in Communications* 8.6 (1990), 948–964.

[5] M. Erhard, R. Fickler, M. Krenn and A. Zeilinger. Twisted Photons: New Quantum Perspectives in High Dimensions. *Nature Publishing Group* 7.3 (2017), 17111–17146. ISSN: 20477538. DOI: 10.1038/lsa.2017.146. eprint: 1708.06101.

[6] N. J. Cerf, M. Bourennane, A. Karlsson and N. Gisin. Security of quantum key distribution using d-level systems. *Physical Review Letters* 88.12 (2002), 127902.

[7] M. Huber and M. Pawłowski. Weak randomness in device-independent quantum key distribution and the advantage of using high-dimensional entanglement. *Physical Review A* 88.3 (2013), 032309.

[8] A. Sit, F. Bouchard, R. Fickler, J. Gagnon-Bischoff, H. Larocque, K. Heshami, D. Elser, C. Peuntinger, K. Günthner, B. Heim et al. High-dimensional intracity quantum cryptography with structured photons. *Optica* 4.9 (2017), 1006–1010.

[9] M. Krenn, J. Handsteiner, M. Fink, R. Fickler and A. Zeilinger. Twisted photon entanglement through turbulent air across Vienna. *Proceedings of the National Academy of Sciences* 112.46 (2015), 14197–14201.

[10] M. Krenn, R. Fickler, M. Fink, J. Handsteiner, M. Malik, T. Scheidl, R. Ursin and A. Zeilinger. Communication with spatially modulated light through turbulent air across Vienna. *New Journal of Physics* 16.11 (2014), 113028.

[11] A. Bocharov, M. Roetteler and K. M. Svore. Factoring with qutrits: Shor's algorithm on ternary and metaplectic quantum architectures. *Physical Review A* 96.1 (2017), 012306.

[12] E. T. Campbell, H. Anwar and D. E. Browne. Magic-state distillation in all prime dimensions using quantum reed-muller codes. *Physical Review X* 2.4 (2012), 041021.

[13] F. Schlederer, M. Krenn, R. Fickler, M. Malik and A. Zeilinger. Cyclic transformation of orbital angular momentum modes. *New Journal of Physics* 18.4 (2016), 043019.

[14] A. Babazadeh, M. Erhard, F. Wang, M. Malik, R. Nouroozi, M. Krenn and A. Zeilinger. High-Dimensional Single-Photon Quantum Gates: Concepts and Experiments. *Phys. Rev. Lett.* 119 (18 Nov. 2017), 180510. DOI: 10.1103/PhysRevLett.119.180510.

[15] G. Labroille, B. Denolle, P. Jian, P. Genevaux, N. Treps and J.-F. Morizur. Efficient and mode selective spatial mode multiplexer based on multi-plane light conversion. *Optics express* 22.13 (2014), 15599–15607.

[16] N. K. Fontaine, R. Ryf, H. Chen, D. Neilson and J. Carpenter. Design of High Order Mode-Multiplexers using Multiplane Light Conversion. *2017 European Conference on Optical Communication (ECOC)*. IEEE, Sept. 2017, 1–3. ISBN: 978-1-5386-5624-2. DOI: 10.1109/ECOC.2017.8346129.

[17] F. Brandt, M. Hiekkamäki, F. Bouchard, M. Huber and R. Fickler. High-dimensional quantum gates using full-field spatial modes of photons. (July 2019). arXiv: 1907.13002.

[18] A. Einstein. Concerning an Heuristic Point of View toward the Emission and Transformation of Light. *Annalen der Physik* 17 (1905), 132–148.

[19] C. Gerry and P. Knight. *Introductory Quantum Optics*. Cambridge University Press, 2004. DOI: 10.1017/CBO9780511791239.

[20] S. Gasiorowicz. *Quantum Physics*. 3rd ed. Wiley, 2003.

[21] T. Durt, B.-G. Englert, I. Bengtsson and K. Życzkowski. On mutually unbiased bases. *International Journal of Quantum Information* 8.4 (Apr. 2010), 535–640. ISSN: 02197499. DOI: 10.1142/S0219749910006502.

[22] J. Binney and D. Skinner. *The physics of quantum mechanics*. Oxford University Press, 2013.

[23] M. Fox. *Quantum optics: an introduction*. Vol. 15. OUP Oxford, 2006.

[24] X. T. Zou and L. Mandel. Photon-antibunching and sub-Poissonian photon statistics. *Phys. Rev. A* 41.1 (1990), 475–476. ISSN: 10502947. DOI: 10.1103/PhysRevA.41.475.

[25] C. Hong and L. Mandel. Experimental realization of a localized one-photon state. *Physical Review Letters* 56.1 (1986), 58.

[26] R. W. Boyd. Nonlinear Optics. Ed. by R. W. Boyd. San Diego: Academic Press, 1992, 1–157. ISBN: 978-0-12-121680-1. DOI: https://doi.org/10.1016/B978-0-12-121680-1.50005-9.

[27] E. Hecht. *Optics*. 5th ed. Pearson Education Ltd, 2017.

[28] P. G. Kwiat, K. Mattle, H. Weinfurter, A. Zeilinger, A. V. Sergienko and Y. Shih. New High-Intensity Source of Polarization-Entangled Photon Pairs. *Phys. Rev. Lett.* 75 (24 Dec. 1995), 4337–4341. DOI: 10.1103/PhysRevLett.75.4337.

[29] L. G. Helt, M. Liscidini and J. E. Sipe. How do they scale?-Classical and quantum nonlinear optical processes in integrated devices. *Optics InfoBase Conference Papers* 29.8 (2012), 2199–2212. ISSN: 21622701.

[30] W. P. Grice and I. A. Walmsley. Spectral information and distinguishability in type-II down-conversion with a broadband pump. *Physical Review A - Atomic, Molecular, and Optical Physics* 56.2 (1997), 1627–1634. ISSN: 10941622. DOI: 10.1103/PhysRevA.56.1627.

[31] J. C. Howell, R. S. Bennink, S. J. Bentley and R. Boyd. Realization of the Einstein-Podolsky-Rosen paradox using momentum-and position-entangled photons from spontaneous parametric down conversion. *Physical Review Letters* 92.21 (2004), 210403.

[32] N. Tischler, A. Büse, L. G. Helt, M. L. Juan, N. Piro, J. Ghosh, M. J. Steel and G. Molina-Terriza. Measurement and Shaping of Biphoton Spectral Wave Functions. *Physical Review Letters* 115.19 (2015), 1–5. ISSN: 10797114. DOI: 10.1103/PhysRevLett.115.193602.

[33] R. L. Byer and S. E. Harris. Power and Bandwidth of Spontaneous Parametric Emission. *Phys. Rev.* 168.3 (1968), 1064–1068. ISSN: 0031899X. DOI: 10.1103/PhysRev.168.1064.

[34] R. Fickler. Entanglement of complex structures of photons. PhD thesis. uniwien, 2014.

[35] M. M. Fejer, G. A. Magel, D. H. Jundt and R. L. Byer. Quasi-phase-matched second harmonic generation: tuning and tolerances. *IEEE Journal of Quantum Electronics* 28.11 (Nov. 1992), 2631–2654. ISSN: 0018-9197. DOI: 10.1109/3.161322.

[36] D. Ljunggren and M. Tengner. Optimal focusing for maximal collection of entangled narrowband photon pairs into single-mode fibers. *Physical Review A* 72.6 (2005), 062301.

[37] N. E. Yu, S. Kurimura, K. Kitamura, J. H. Ro, M. Cha, S. Ashihara, T. Shimura, K. Kuroda and T. Taira. Efficient frequency doubling of a femtosecond pulse with simultaneous group-velocity matching and quasi phase matching in periodically poled, MgO-doped lithium niobate. *Applied physics letters* 82.20 (2003), 3388–3390.

[38] S. Emanueli and A. Arie. Temperature-dependent dispersion equations for KTiOPO4 and KTiOAsO4. *Appl. Opt.* 42.33 (Nov. 2003), 6661–6665. DOI: 10.1364/AO.42.006661.

[39] A. Fedrizzi, T. Herbst, A. Poppe, T. Jennewein and A. Zeilinger. A wavelength-tunable fiber-coupled source of narrowband entangled photons. *Optics Express* 15.23 (2007), 15377–15386.

[40] R. Ghosh, C. K. Hong, Z. Y. Ou and L. Mandel. Interference of two photons in parametric down conversion. *Phys. Rev. A* 34 (5 Nov. 1986), 3962–3968. DOI: 10.1103/PhysRevA.34.3962.

[41] A. M. Brańczyk. Hong-Ou-Mandel Interference. (2017), 1–17. ISSN: 00220418. arXiv: 1711.00080.

[42] C. K. Hong, Z. Y. Ou and L. Mandel. Measurement of subpicosecond time intervals between two photons by interference. *Phys. Rev. Lett.* 59.18 (1987), 2044–2046. DOI: 10.1103/PhysRevLett.59.2044.

[43] N. K. Langford, T. Weinhold, R. Prevedel, K. Resch, A. Gilchrist, J. O'Brien, G. Pryde and A. White. Demonstration of a simple entangling optical gate and its use in Bell-state analysis. *Physical Review Letters* 95.21 (2005), 210504.

[44] C. Lang, C. Eichler, L. Steffen, J. Fink, M. Woolley, A. Blais and A. Wallraff. Correlations, indistinguishability and entanglement in Hong–Ou–Mandel experiments at microwave frequencies. *Nature Physics* 9.6 (2013), 345.

[45] K. N. Cassemiro, K. Laiho and C. Silberhorn. Accessing the purity of a single photon by the width of the Hong–Ou–Mandel interference. *New Journal of Physics* 12.11 (2010), 113052.

[46] F. U. Klauck, L. Teuber, M. Ornigotti, M. Heinrich, S. Scheel and A. Szameit. Observation of PT-symmetric quantum interference. *arXiv preprint arXiv:1904.08135* (2019).

[47] D. L. Andrews and M. Babiker. *The angular momentum of light*. Cambridge University Press, 2012.

[48] E. W. Weisstein. *Associated Laguerre Polynomial.* URL: http://mathworld.wolfram.com/AssociatedLaguerrePolynomial.html.

[49] E. Bolduc, N. Bent, E. Santamato, E. Karimi and R. W. Boyd. Exact solution to simultaneous intensity and phase encryption with a single phase-only hologram. *Opt. Lett.* 38.18 (2013), 3546–3549. DOI: 10.1364/OL.38.003546.

[50] F. Bouchard, N. H. Valencia, F. Brandt, R. Fickler, M. Huber, M. Malik, N. Herrera Valencia, F. Brandt, R. Fickler, M. Huber and M. Malik. Measuring azimuthal and radial modes of photons. 26.24 (2018), 31925–31941. DOI: 10.1364/OE.26.031925.

[51] N. Bozinovic, Y. Yue, Y. Ren, M. Tur, P. Kristensen, H. Huang, A. E. Willner and S. Ramachandran. Terabit-Scale Orbital Angular Momentum Mode Division Multiplexing in Fibers. *Science* 340 (2013), 1545–1548.

[52] A. M. Yao and M. J. Padgett. Orbital angular momentum: origins, behavior and applications. *Advances in Optics and Photonics* 3.2 (2011), 161–204. DOI: 10.1364/AOP.3.000161.

[53] A. Mair, A. Vaziri, G. Weihs and A. Zeilinger. Entanglement of the orbital angular momentum states of photons. *Nature* 412.6844 (2001), 313.

[54] M. Mafu, A. Dudley, S. Goyal, D. Giovannini, M. McLaren, M. J. Padgett, T. Konrad, F. Petruccione, N. Lütkenhaus and A. Forbes. Higher-dimensional orbital-angular-momentum-based quantum key distribution with mutually unbiased bases. *Physical Review A* 88.3 (2013), 032305.

[55] Generation of high-order Hermite-Gaussian modes in end-pumped solid-state lasers for square vortex array laser beam generation. *Optics Express* 20.7 (2012), 7128.

[56] T. Hashimoto, T. Saida, I. Ogawa, M. Kohtoku, T. Shibata and H. Takahashi. Optical circuit design based on a wavefront-matching method. *Optics Letters* 30 (2005), 2620.

[57] J. W. Goodman. *Introduction to Fourier Optics*. 1996.

[58] G. Ruffato, M. Massari, G. Parisi and F. Romanato. Test of mode-division multiplexing and demultiplexing in free-space with diffractive transformation optics. *Optics Express* 25 (2017), 7859–7868.

[59] L. Hu, L. Xuan, Y. Liu, Z. Cao, D. Li and Q. Mu. Phase-only liquid crystal spatial light modulator for wavefront correction with high precision. *Optics Express* 12.26 (2004), 6403. DOI: 10.1364/opex.12.006403.

[60] K. Lu. Determination of the physical properties of an arbitrary twisted-nematic liquid crystal cell. *Optical Engineering* 33.8 (1994), 2704. ISSN: 0091-3286. DOI: 10.1117/12.173544.

[61] *Phase spatial light modulator LCOS-SLM*. https://www.hamamatsu.com/resources/pdf/ssd/e12_handbook_lcos_slm.pdf. Accessed: 24.09.2019.

[62] A. Mair, A. Vaziri, G. Weihs and A. Zeilinger. Entanglement of the orbital angular momentum states of photons. *Nature* 412.6844 (2001), 313–316. ISSN: 1476-4687. DOI: 10.1038/35085529.

[63] V. Bazhenov, M. Vasnetsov and M. Soskin. Laser beams with screw dislocations in their wavefonts. *Optical and Quantum Electronics* 24 (Jan. 1990), 951–962.

[64] M. Krenn, M. Malik, M. Erhard, A. Zeilinger, A. Soc and M. Krenn. Orbital angular momentum of photons and the entanglement of Laguerre – Gaussian modes Subject Areas :

Authors for correspondence : *Philosophical Transactions of the Royal Society A: Mathematical, Physical and Engineering Sciences* (2017). ISSN: 1364503X. DOI: 10.1098/rsta.2015.0442. eprint: 1607.05114.

[65] M. Mafu, A. Dudley, S. Goyal, D. Giovannini, M. McLaren, M. J. Padgett, T. Konrad, F. Petruccione, N. Lütkenhaus and A. Forbes. Higher-dimensional orbital angular momentum based quantum key distribution with mutually unbiased bases. *Physical Review A - Atomic, Molecular, and Optical Physics* 88.3 (Feb. 2014), 1–9. ISSN: 10502947. DOI: 10.1103/PhysRevA.88.032305.

[66] C. H. Bennett and G. Brassard. Quantum cryptography: Public key distribution and coin tossing. *Theoretical Computer Science* 560 (Dec. 2014), 7–11. ISSN: 0304-3975. DOI: 10.1016/J.TCS.2014.05.025.

[67] L. Sheridan and V. Scarani. Security proof for quantum key distribution using qudit systems. *Phys. Rev. A* 82 (3 Sept. 2010), 030301. DOI: 10.1103/PhysRevA.82.030301.

[68] R. Schmied. Quantum state tomography of a single qubit: comparison of methods. *Journal of Modern Optics* 63.18 (2016), 1744–1758. DOI: 10.1080/09500340.2016.1142018.

[69] K. S. Kravtsov, S. S. Straupe, I. V. Radchenko, N. M. T. Houlsby, F. Huszár and S. P. Kulik. Experimental adaptive Bayesian tomography. *Phys. Rev. A* 87.6 (2013), 62122. ISSN: 10502947. DOI: 10.1103/PhysRevA.87.062122.

[70] C. Schwemmer, L. Knips, D. Richart, H. Weinfurter, T. Moroder, M. Kleinmann and O. Gühne. Systematic Errors in Current Quantum State Tomography Tools. *Physical Review Letters* 114.8 (Feb. 2015), 080403. ISSN: 0031-9007. DOI: 10.1103/PhysRevLett.114.080403.

[71] A. Gilchrist, N. K. Langford and M. A. Nielsen. Distance measures to compare real and ideal quantum processes. *Phys. Rev. A* 71 (6 June 2005), 062310. DOI: 10.1103/PhysRevA.71.062310.

[72] A. M. Yao. Angular momentum decomposition of entangled photons with an arbitrary pump. *New Journal of Physics* 13.5 (2011), 053048.

[73] A. Büse, N. Tischler, M. L. Juan and G. Molina-Terriza. Where are photons created in parametric down-conversion? on the control of the spatio-temporal properties of biphoton states. *Journal of Optics (United Kingdom)* 17.6 (2015). ISSN: 20408986. DOI: 10.1088/2040-8978/17/6/065201.

[74] R. S. Bennink. Optimal collinear Gaussian beams for spontaneous parametric down-conversion. *Physical Review A* 81.5 (2010), 053805.

[75] C. I. Osorio, A. Valencia and J. P. Torres. Spatiotemporal correlations in entangled photons generated by spontaneous parametric down conversion. *New Journal of Physics* 10.11 (2008), 113012.

[76] Z.-Y. J. Ou. *Multi-photon quantum interference*. Vol. 43. Springer, 2007.

[77] G. Weihs, M. Reck, H. Weinfurter and A. Zeilinger. Two-photon interference in optical fiber multiports. *Physical Review A* 54.1 (1996), 893.